Disentangling impact ejecta dynamics using micro–X-ray fluorescence (µ-XRF): a case study from the terrestrial Cretaceous-Paleogene (K-Pg) boundary

Pim Kaskes[1,2], Roald Tagle[3], Mariia Rey[1], Steven Goderis[1], Sophie Decrée[4], Jan Smit[5], and Philippe Claeys[1]

[1] *Archaeology, Environmental Changes & Geo-Chemistry (AMGC), Vrije Universiteit Brussel, Pleinlaan 2, 1050 Brussels, Belgium.*
[2] *Laboratoire G-Time, Université Libre de Bruxelles, Av. F.D. Roosevelt 50, 1050 Brussels, Belgium.*
[3] *Bruker Nano Analytics GmbH, Am Studio 2d, 12489 Berlin, Germany.*
[4] *Institute of Natural Sciences – Geological Survey of Belgium, Vautierstraat 29, 1000, Brussels, Belgium.*
[5] *Department of Earth Sciences, Vrije Universiteit Amsterdam, De Boelelaan 1085, 1081 HV Amsterdam, Netherlands.*

Corresponding author: Pim Kaskes (pim.kaskes@vub.be)

Peer review status:

This is a non-peer-reviewed pre-print submitted to EarthArXiv. This manuscript has been submitted in December 2024 for publication in the journal *Geochemistry, Geophysics, Geosystems*.

Key Points:

- Micro-X-ray fluorescence offers a well-suited high-resolution mapping tool for event deposits such as the Cretaceous-Paleogene boundary.
- Geochemical profiles from the Raton Basin (USA) shed new light on ejecta dynamics in the first minutes to years post-Chicxulub impact.
- Prominent enrichments in both zirconium and chromium are linked to the slow atmospheric settling of the Chicxulub impact dust plume.

Abstract

This study presents a non-destructive geochemical and petrographic workflow to generate high-resolution chemostratigraphic records across key stratigraphic intervals, here exemplified by a terrestrial Cretaceous-Paleogene (K-Pg) boundary sequence. The geochemical records fingerprint specific Chicxulub related impact ejecta products and thereby further constrain the timeline of ejecta deposition. High-resolution (25 µm) micro-X-ray fluorescence (µ-XRF) mapping and quantitative integrated-area linescans in combination with ESEM-EDS analyses of the Starkville South sequence (Raton Basin, Colorado) reveal a complex microstratigraphy, in which additional sublayers can be identified than the classic 'dual-layer' succession, described in literature for US Western Interior K-Pg sites. First, a basal claystone is identified with abundant glassy impact spherules that have been altered over time to kaolinite and jarosite due to acidic and reducing conditions in a local swamp environment. This first lithology is followed by a carbonaceous shale interval rich in ejected quartz grains. These two ejecta intervals are interpreted to have formed by ballistic transport from the Chicxulub crater region and were likely emplaced within ∼1 hour after impact at Starkville. In the overlying lignite layer, pronounced enrichments in both zirconium and chromium are detected, hinting to a triple ejecta layer with a large part of the siderophile element anomaly being likely preserved in this coaly interval, including the famous iridium anomaly. These enrichments are attributed to fine-grained impact dust comprising of pulverized granitoid basement (Zr) and an admixture of meteoritic material (Cr, Ni and likely Ir), probably deposited <20 years after impact following slow atmospheric settling.

Plain Language Summary

This study uses advanced geochemical mapping to analyze layers of debris derived from the Chicxulub asteroid impact, linked to the dinosaur mass extinction 66 million years ago. In sediments from the Raton Basin (Colorado, USA), we identified three sublayers containing Chicxulub impact materials. These are altered melt spherules and ejected mineral grains that were rapidly formed after impact, followed by a layer of ultrafine dust consisting of pulverized granite and meteorite material that settled slowly out of the atmosphere. Our high-resolution geochemical workflow offers new insights into the timing and mechanisms of ejecta production, transport and deposition after a large meteorite impact event.

1 Introduction

The Chicxulub hypervelocity impact event on Earth ~66 Myr ago represents an ideal case-study to better understand cratering processes on Earth and in the Solar System (Alvarez et al., 1980; Smit and Hertogen, 1980; Kring et al., 2017; Morgan et al., 2022). A key element is the reconstruction of the processes related to impact ejecta production, transport, and deposition (Alvarez et al., 1995; Smit, 1999; Claeys et al., 2002; Artemieva and Morgan, 2009; Schulte et al., 2010). The ~200-km-wide Chicxulub impact structure on the Yucatán Peninsula (Mexico) is unique (Hildebrand et al., 1991) as it is the only terrestrial impact structure with ejecta preserved worldwide, which allows for a direct comparison between material from the source area (Kring and Boynton, 1992; Swisher et al., 1992; Feignon et al., 2020; de Graaff et al., 2022; Kaskes et al., 2024) and its global deposits (Bohor et al., 1987; Kamo and Krogh, 1995; Claeys et al., 2002). High-resolution geochemical and petrographic analysis across these globally distributed Cretaceous-Paleogene (K-Pg) boundary event deposits is crucial to disentangle the sequence of geological and biological events that occurred prior to and in the direct aftermath of the Chicxulub impact event, including the dynamics related to the K-Pg boundary mass extinction (Kring, 2007; Schulte et al., 2010; Morgan et al., 2022; Senel et al., 2023). Recent sedimentological analysis of highly expanded K-Pg boundary successions from within the Chicxulub impact structure (Gulick et al., 2019; Kaskes et al., 2022) and from North-Dakota (DePalma et al., 2019; Senel et al., 2023) make it possible to reconstruct impact cratering processes at an unparalleled resolution of hours to days after impact.

The terrestrial K-Pg boundary sites in the US Western Interior (Fig. 1A) are ideal candidates to further unravel the mechanisms and timing of Chicxulub impact ejecta distribution and deposition in the first moments after impact. In contrast to the thick (>1 dm) but high-energy, marine K-Pg deposits around the Gulf of Mexico (at < 1500 km paleodistance to the Chicxulub structure; Smit et al., 1992b; Arz et al., 2022), the paludal Western Interior K-Pg localities have preserved a non-disturbed chronological record of the ejecta sedimentation because the material did not settle through a thick water column (Izett, 1990). In addition, the intermediate paleodistance to the Chicxulub impact structure (2000-3000 km) accounts for a boundary sequence of 1-3 cm thick, thereby providing a much higher temporal resolution compared to the often condensed and thin (< 1 cm) distal K-Pg boundaries at > 5000 km paleodistance to Chicxulub (Smit, 1999; Schulte et al., 2010).

Over the last decade, the rapid development of *in-situ* chemical and petrographic techniques at the micro- to even nanoscale makes it possible to analyze and visualize compositional variations at an ultra-high stratigraphic resolution and accuracy. This progress opens a number of opportunities to reconstruct key moments in the early history of abrupt geological processes such as hypervelocity impact events like Chicxulub. High-resolution, (near-)continuous datasets from well-preserved K-Pg impact ejecta sequences shed light on the nature and chronology of Chicxulub ejecta products, such as impact spherules (microtektites and microkrystites; (Smit et al., 1992a; Belza et al., 2017)), shocked minerals (Bohor et al., 1984; Bohor et al., 1993), Ni-rich spinels (Robin et al., 1992) and/or iridium rich dust (Alvarez et al., 1980; Smit and Hertogen, 1980; Goderis et al., 2013; Goderis et al., 2021), and may therefore assist in groundtruthing ejecta emplacement models (Artemieva and Morgan, 2009; Artemieva and Morgan, 2020).

This study presents the results of high-resolution micro-X-ray fluorescence (µ-XRF) analysis integrated with scanning electron microscopy on a K-Pg boundary microstratigraphy from the Raton Basin (USA), typical for the US Western Interior intermediate K-Pg sites, to elucidate the complex processes of ejecta transport and deposition linked to the Chicxulub impact event. The novel, non-destructive µ-XRF workflow proposed here, also opens windows to characterize impact ejecta sequences related to other impact structures and to investigate at (sub-)centimeter resolution key stratigraphic intervals in general.

2 Geological setting

The K-Pg boundary deposits from the Raton Basin in the border region between Colorado and New Mexico (USA; Fig. 1B), located in a 6400 km^2 wide asymmetric structural depression are the most proximal terrestrial K-Pg localities that preserved large quantities of relatively well-preserved Chicxulub impact ejecta material (Orth et al., 1981; Pillmore et al., 1984). The paleodistance from the Raton Basin to the center of the Chicxulub impact structure is estimated to be in between 2100 and 2250 km (Schulte et al., 2010). The Upper Cretaceous to Paleocene stratigraphy in the Raton Basin reflects a regressive sequence consisting mainly of thick packages of siliciclastic deposition at the edge of the retreating Cretaceous Western Interior Seaway (Pillmore and Flores, 1987).

The Campanian marine Pierre Shale is followed stratigraphically by the characteristic cliff-forming Trinidad Sandstone, a 25-30 m thick tabular sandstone unit reflecting coastal barrier-bar environments during the eastward progradation of the Upper Cretaceous coastline (Fig. 1B) (Pillmore et al., 1984). This unit is conformably overlain by the fine-grained siliciclastic Vermejo Formation (Maastrichtian) followed by an erosional unconformity at the base of the Raton Formation (Maastrichtian-Danian). This formation comprises conglomerate, sandstone, siltstone, mudstone and coal intervals, and its thickness ranges from 335 m in the eastern part of the Raton Basin to more than 600 m in the west-central region (Pillmore et al., 1984). The K-Pg boundary layer is located in the lower part of the Raton Formation, near the top of the lower coal zone beneath a cliff-forming series of predominantly channel sandstones (Pillmore et al., 1984). The depositional environment of this part of the Raton Formation is interpreted to represent an ever-wet environment containing a combination of meandering channels with low-lying floodplains and local backswamps, where crevasse splays periodically interrupted the deposition of organic material (Pillmore and Flores, 1987; Schwartz et al., 2021). These quiet, freshwater, coal swamp conditions extended over a broad alluvial plain and represented an ideal environment to receive and preserve the fallout of impact ejecta related to the Chicxulub impact event (Sharpton et al., 1990).

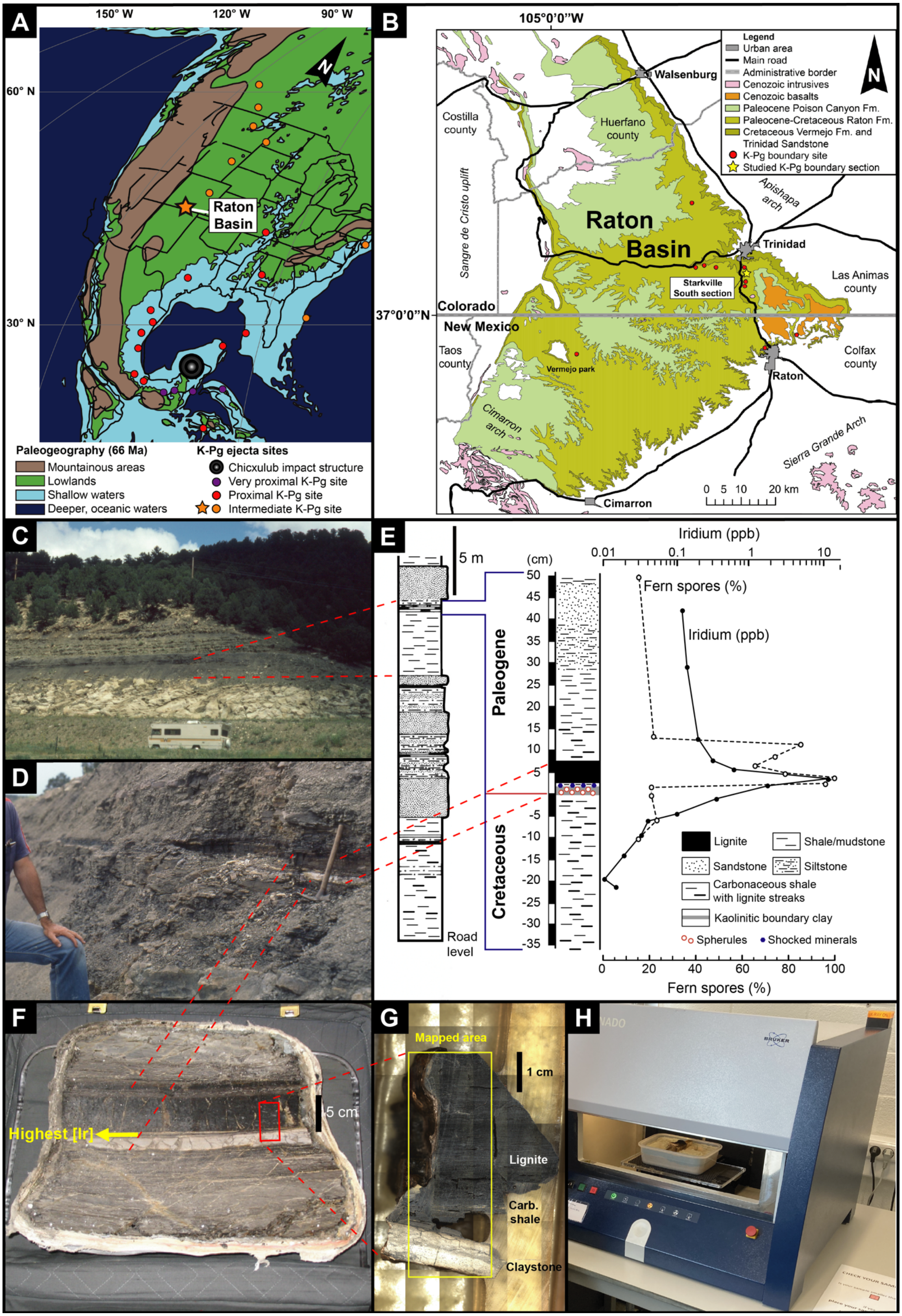
A
150° W
120° W
90° W
60° N
30° N
N
Raton Basin
Paleogeography (66 Ma)
Mountainous areas
Lowlands
Shallow waters
Deeper, oceanic waters
K-Pg ejecta sites
Chicxulub impact structure
Very proximal K-Pg site
Proximal K-Pg site
Intermediate K-Pg site
B
105°0'0"W
Legend
Urban area
Main road
Administrative border
Cenozoic intrusives
Cenozoic basalts
Paleocene Poison Canyon Fm.
Paleocene-Cretaceous Raton Fm.
Cretaceous Vermejo Fm. and Trinidad Sandstone
K-Pg boundary site
Studied K-Pg boundary section
Walsenburg
Costilla county
Huerfano county
Sangre de Cristo uplift
Apishapa arch
Raton Basin
Trinidad
Starkville South section
Las Animas county
Colorado
37°0'0"N
New Mexico
Taos county
Vermejo park
Colfax county
Raton
Cimarron arch
Sierra Grande Arch
0 5 10 20 km
Cimarron
C
D
E
5 m
Road level
Paleogene
Cretaceous
(cm)
Iridium (ppb)
0.01 0.1 1 10
Fern spores (%)
Iridium (ppb)
Lignite
Shale/mudstone
Sandstone
Siltstone
Carbonaceous shale with lignite streaks
Kaolinitic boundary clay
Spherules
Shocked minerals
0 20 40 60 80 100
Fern spores (%)
F
Highest [Ir]
5 cm
G
Mapped area
1 cm
Lignite
Carb. shale
Claystone
H

Figure 1. Geological context of the Starkville-South K-Pg boundary site (SVS). (A) Paleogeographic map of northern America during the latest Cretaceous, highlighting the Raton Basin, the Chicxulub impact structure and other (very proximal to intermediate) K-Pg localities (adapted from Claeys et al., 2002; Scotese, 2004; Schulte et al., 2010; Snedden and Galloway, 2019; Goderis et al., 2021). **(B)** Simplified geological map of the Raton Basin in New Mexico and Colorado displaying the location of SVS and other neighboring K-Pg boundary sites. Geological map adapted from Tweto (1979) and Hoffman and Jopnes (2005). K-Pg boundary localities from Pillmore et al. (1984). **(C-D)** Field photos showing a succession of the lower coal zone of the Raton Formation with a prominent channel sandstone, a mudstone evolving into a carbonaceous shale, then a prominent pink kaolinitic tonstein, darkgrey carbonaceous shale, followed by a lignite interval. Camper van and hammer for scale (pictures by Jan Smit). **(E)** Schematic lithology of Starkville with iridium concentrations (black circles) and percentages of fern spores (open circles). The highest iridium concentrations documented in literature for Starkville are found at the boundary between the upper part of the boundary claystone (the 'fireball layer' rich in shocked minerals) and the overlying lignite, as indicated schematically also with a yellow arrow in F. The fern spike consists predominantly of the trilete fern species *Cyathidites diaphana* (adapted from Pillmore & Flores, 1987; Tschudy et al., 1984; Schulte et al., 2010). **(F)** Plaster-jacketed block yielding the SVS K-Pg boundary stratigraphy, currently on display at the Rieskrater Museum in Nördlingen, Germany (Berlin et al., 2010), with highest iridium concentrations from literature projected on the sample. **(G)** Mosaic-scan of the small epoxy resin block cut out of the block from F, the yellow rectangle indicates the mapped surface for the µ-XRF analysis. **(H)** Laboratory setup at the Vrije Universiteit Brussel for the µ-XRF analyses on the horizontally oriented SVS K-Pg epoxy slab using a Bruker M4 Tornado µ-XRF instrument.

This study focuses specifically on the Starkville South K-Pg site (SVS; Fig. 1B-E) in southern Colorado because the lithology at this site is well-described in literature as characteristic for the Raton Basin (Pillmore et al., 1984; Pillmore and Flores, 1987; Pollastro and Pillmore, 1987). The clastic fraction of this section is regarded as relatively unaltered with abundant impact-related minerals (e.g., shocked quartz, feldspar) preserved (Sharpton et al., 1990), and its boundary claystone interval is characterized by highly elevated iridium concentrations between 16-56 ppb (Pillmore et al., 1984; Goderis et al., 2013) (Fig. 1E), which highlights the presence of geochemical traces of Chicxulub impact ejecta products. The basal part of a lignite overlying the boundary clay interval is also characterized by a pronounced fern spike, a clear marker for the K-Pg mass extinction horizon (Tschudy et al., 1984) (Fig. 1E). The section at SVS consists of ~25 m stratigraphy (Pillmore & Flores, 1987), comprising a prominent channel sandstone, a mudstone evolving into a carbonaceous shale, followed by a prominent pinkish kaolinitic tonstein and a darkgrey carbonaceous shale that transitions into a Paleocene lignite interval (Fig. 1C-G). SVS is situated in a roadcut ∼4 km south of the exit to the town of Starkville from the Interstate Highway 25, southern Colorado (37°5'57.30"N; 104°31'14.50"W). Geochemical and petrographic analysis of SVS has so far mostly focused on the pink kaolinite layer and on bulk samples at a centimeter to millimeter stratigraphic sampling (Sharpton et al., 1990; Pillmore et al., 1984; Pollastro & Pillmore, 1987; Izett, 1990). Here, the main focus lies on the sedimentary sequence directly above the kaolinitic claystone. A multi-proxy workflow at a micrometer-scale resolution is introduced to identify the ejecta components and to unravel the depositional processes of the SVS K-Pg event stratigraphy.

3 Materials and Methods

In 2005, researchers from the University of New Mexico excavated a large K-Pg boundary block from the Starkville-South K-Pg site (Berlin et al., 2010), which is currently on display in the Rieskrater Museum (Nördlingen, Germany). This sample was stabilized with plaster of Paris and epoxy, and was subsequently cut and polished, preserving a continuous ~25 cm thick microstratigraphic succession of an Upper Cretaceous silt- to claystone, a K-Pg boundary interval of kaolinitic clay and carbonaceous shale, and a Paleocene lignite (Fig. 1F). A representative subsample from this resin block (~3 x 5 cm in size), comprising the kaolinitic tonstein to lignitic part of the K-Pg boundary complex (Fig. 1G), was selected to study in a non-destructive manner the geochemistry and petrography of SVS at a high spatial resolution of 25 µm. As only this embedded block was available for study, no destructive bulk geochemical analysis was possible, and no thin sections were made, for example to study the potential presence of shock features within ejected grains.

3.1 Micro-X-ray fluorescence

The major and trace element composition of the SVS resin slab was determined using energy-dispersive micro-X-ray fluorescence (µ-XRF) scanning at the Vrije Universiteit Brussel, Belgium (VUB), and at Bruker nano GmbH in Berlin, Germany. For this purpose, an M4 TORNADO benchtop µ-XRF surface scanner (Bruker nano GmbH, Berlin, Germany) equipped with a Rh tube as X-ray source, a focusing polycapillary lens (20 µm for Mo Kα) and two XFlash 430 Silicon Drift detectors was used (Fig. 1H). This flexible technique allows to obtain high-resolution elemental distributions by scanning flat sample surfaces in a rapid, non-destructive, and cost-efficient manner (de Winter and Claeys, 2017; Wouters et al., 2020; Kaskes et al., 2021). As the sample contained an abundant hydrocarbon fraction which causes a higher attenuation depth for the X-rays (Kaskes et al., 2021), the µ-XRF mapping was performed using both detectors at intermediate X-ray source energy settings (50 kV and 300 µA) and with the sample oriented horizontally in the vacuum chamber. This orientation was selected to avoid sample material being excited at a higher stratigraphic interval, invoking potential shifts in the chemostratigraphy caused by the oblique incident X-ray beams and the higher attenuation depth of the organic material. The measurements were carried out under near vacuum conditions (20 mbar) with a pixel size resolution of 25 µm and integration time of 50 ms per pixel. This allowed to generate elemental distribution maps; multi-element maps and single-element heatmaps (Fig. 2) in which the color intensity is directly correlated with the intensity of the characteristic element signal per given pixel. To convert the element distribution maps into continuous line profiles, the data was extracted from two subareas with a continuous stratigraphy. This work was done using the linescan function integrated into the M4 TORNADO Software. The extracted data allowed to produce two partly overlapping chemical profiles of the K-Pg boundary interval at 25 µm stratigraphic resolution, which are hereafter termed integrated-area linescans (IAL; i.e. IAL-1 and IAL-2).

To obtain quantitative µ-XRF linescans, 15 (nanometer-milled) pressed powder pellets of certified geological reference materials (provided by myStandards GmbH, Kiel, Germany) are measured by applying repeated µ-XRF spot analyses (n = 3 per standard) using the same settings as the mapping described above, but with an acquisition time of 240 s (real-time) per 25 µm pixel size. A similar nano-particulate pressed powder pellet (NIOZ Foraminifera House Standard-2-Nano-Pellet) has recently been developed and tested for a satisfactory homogeneous composition, which resulted in various paleoclimate research applications (Boer et al., 2022). The 15 nano-pellets consist of certified reference materials that range from felsic and mafic igneous rocks to carbonates (details in Table 1; values obtained from the GeoREM database (Jochum et al., 2005)). The first quantification of the XRF spectra is performed by using the fundamental parameters algorithm (Rousseau, 1984a; Rousseau, 1984b; Rousseau and Bouchard, 1986) integrated in the M4 TORNADO µ-XRF software, which is based on the theoretical Sherman equation (Sherman, 1955) that allows to infer from the measured spectra the respective elemental concentrations (De Winter et al., 2017). The quantification results (in non-normalized oxides wt%) of the 15 reference samples were plotted versus the reference values, to obtain the sensitivity correction (slope) and potential intercept value required to quantify the unknown sample. The results in Fig. 4, show all a very good linear correlation ($R^2 > 0.99$). This method of standard supported fundamental parameter quantification not only allows to improve the analytical results but serves also as a validation. All chemical profile data of IAL-1 and IAL-2 can be found in Supplementary Table S1, and is plotted in Fig. 5 and Fig. S3.

3.2 Scanning electron microscopy

Detailed petrographic examination of the SVS slab (Fig. 3) is carried out using a Quanta 20 (FEI Company, Hillsboro, USA) low vacuum environmental scanning electron microscope (ESEM) at the Institute of Natural Sciences, Brussels, Belgium (RBINS) (Decrée et al., 2020). For this study, environmental SEM is preferred because of the large mounting stage (L x W x H: 14 x 6 x 4 cm) and the ability to visualize microtextures in an organic-rich sample while avoiding the use of a carbon coating. The ESEM at the RBINS is equipped with an Apollo 10 Silicon Drift energy dispersive X-ray spectrometer (EDS; EDAX, Pleasanton, USA), which is used to verify the composition of mineral and ejecta phases using qualitative spot analyses on backscatter electron (BSE) images.

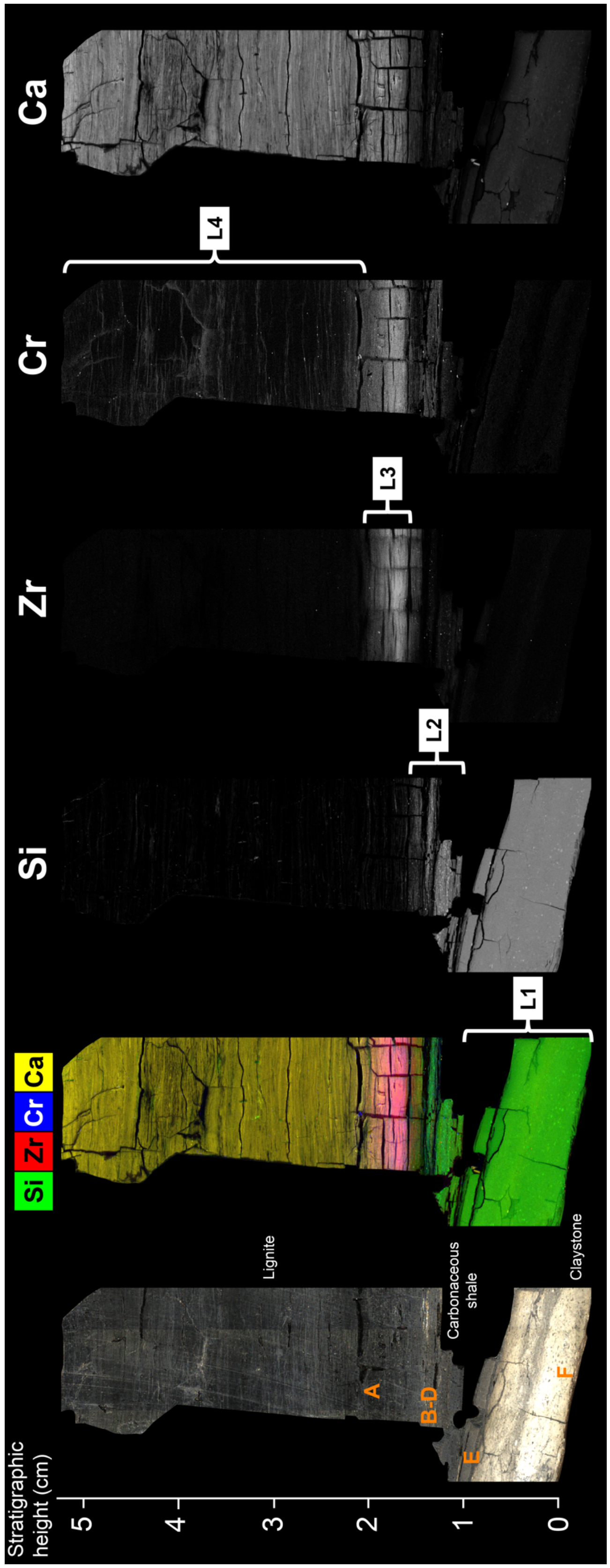
Stratigraphic height (cm)
5
4
3
2
1
0
Lignite
Carbonaceous shale
Claystone
A
B-D
E
F
Si
Zr
Cr
Ca
L1
L2
L3
L4
Si
Zr
Cr
Ca

Figure 2. Overview of elemental distributions. Multi-element µ-XRF map of Si (green), Zr (red), Cr (blue) and Ca (yellow), and semi-quantitative, single-element heat-maps for Si, Zr, Cr, and Ca, displayed with deconvoluted settings. Based on geochemical and petrographic observations, the SVS microstratigraphy is divided into four sublayers (L1-L4) marked on the maps. The letters A-F on the optical image refer to the ESEM-BSE images shown in Fig. 3. Additional single-element heatmaps are shown in Fig. S1.

4 Results

The µ-XRF mapping of the SVS slab detected 32 elements (Fig. S1), namely: Na, Mg, Al, Si, P, S, Cl, K, Ca, Ti, V, Cr, Mn, Fe, Co, Ni, Cu, Zn, Ga, Ge, As, Rb, Sr, Y, Zr, Nb, Mo, Ba, Pb, Th, and U, and Rh (linked to Rh tube). Of this list of major and trace elements, P, S, As, Co, Ge, Mo, Pb, Th, U and Rh could not be quantified accurately based on the matrix-matched multi-standard calibrations of nanopowdered pressed pellets of certified reference materials (Figs. 4; S2). The calibration protocol relying on non-normalized mass concentrations resulted in a slightly better coefficient of determination (R^2) and more realistic slope values than the net intensity approach, so the quantifications using the exported mass concentrations from the Bruker M4 software based on the fundamental parameters method are used. Using this method, R^2 values are > 0.99 for Na_2O, MgO, Al_2O_3, SiO_2, K_2O, CaO, TiO_2, MnO, Fe_2O_3, Cl, V, Cr, Ni, Cu, Zn, Ga, Rb, Sr, Y, Zr, Nb, and Ba (Table 2). Key major oxides and trace elements for the identification of impact ejecta products and intervals represent SiO_2 (potentially linked to ejected quartz grains: Bohor et al., 1984), Al_2O_3 and K_2O (clay components: Pollastro and Pillmore, 1987), Zr (e.g., ejected zircon: Krogh et al., 1993a), Cr and Ni (for Ni-rich spinels (Robin et al., 1992), microkrystites (Belza et al., 2017), and for an admixed meteoritic component (Goderis et al., 2013)). The results of the integrated area linescan (IAL) quantifications are discussed below and are shown in Fig. 5 (for SiO_2, Zr, Cr and Ni profiles) and Fig. S3 for all major and trace element profiles.

By focusing primarily on the distribution and IAL-based chemical profiles of SiO_2, Zr, Cr and Ni, and using a verification by ESEM-EDS, the K-Pg boundary interval is divided into four distinct layers (Figs. 2 and 5). The lowermost stratum (L1: > 0.98 cm thick) represents a claystone that is relatively homogeneous in composition showing consistently high SiO_2 (~53 wt%) and Al_2O_3 contents (~37 wt%) (Fig. 2), and relatively low K_2O (generally < 1 wt%), Zr and Cr concentrations (both < 100 ppm) and very low Ni concentrations (< 12 ppm). ESEM-EDS analysis showed that this layer yields altered impact spherules (Fig. 3E-F). The overlying carbonaceous shale layer (L2: ~5.5 mm thick, from ~0.98 –1.53 cm stratigraphic height) has clear hotspots enriched in both SiO_2 (up to 51 wt%) and Zr (first clear Zr hotspot of 428 ppm at 0.98 cm stratigraphic height; highest Zr hotspot value of 801 ppm at 1.5025 cm height) (Fig. 2), and contains granular petrographic features with ejected quartz and feldspar grains as evidenced by ESEM-EDS (Fig. 3B-D). L2 also shows some elevated peaks in Cr values (on average 120 ppm with a maximum value up to 630 ppm at 1.155 cm height) and a very small number of peaks with Ni enrichments (one peak up to 90 ppm). The highest bulk iridium values available in literature for Starkville

South (56 ppb) is observed in this layer with ejected shocked mineral grains (Pillmore et al., 1984), which corresponds to L2 in this study. The third layer (L3: ~8.2 mm thick from ~1.53 - 2.35 cm) is a transition interval from carbonaceous shale to lignite (Fig. 3A) and is characterized by low SiO_2 values (< 25 wt% with on average 11.7 wt%), and a sharp peak with both very high concentrations of Zr (maximum value of 3984 ppm at 1.79 cm stratigraphic height) and Cr (maximum value of 839 ppm at 1.71 cm height). Ni also shows clear enrichments in this interval, with a maximum value of 474 ppm Ni located at 2.065 cm stratigraphic height (Fig. 5). Above 2.35 cm stratigraphic height, the Zr concentrations drop consistently below detection limits (> 44 ppm), which we therefore link to the presence of a fourth layer (L4: > 3 cm thick; from ~2.35 cm upwards). This is a lignite that yields, besides a low Zr content, also low SiO_2 values (on average 8.7 wt%, with a maximum up to 11.5 wt%), and low Cr concentrations (< 200 ppm; on average 11 ppm Cr). In contrast, L4 displays large variations in Ni with high values up to 455 ppm (Fig. 5).

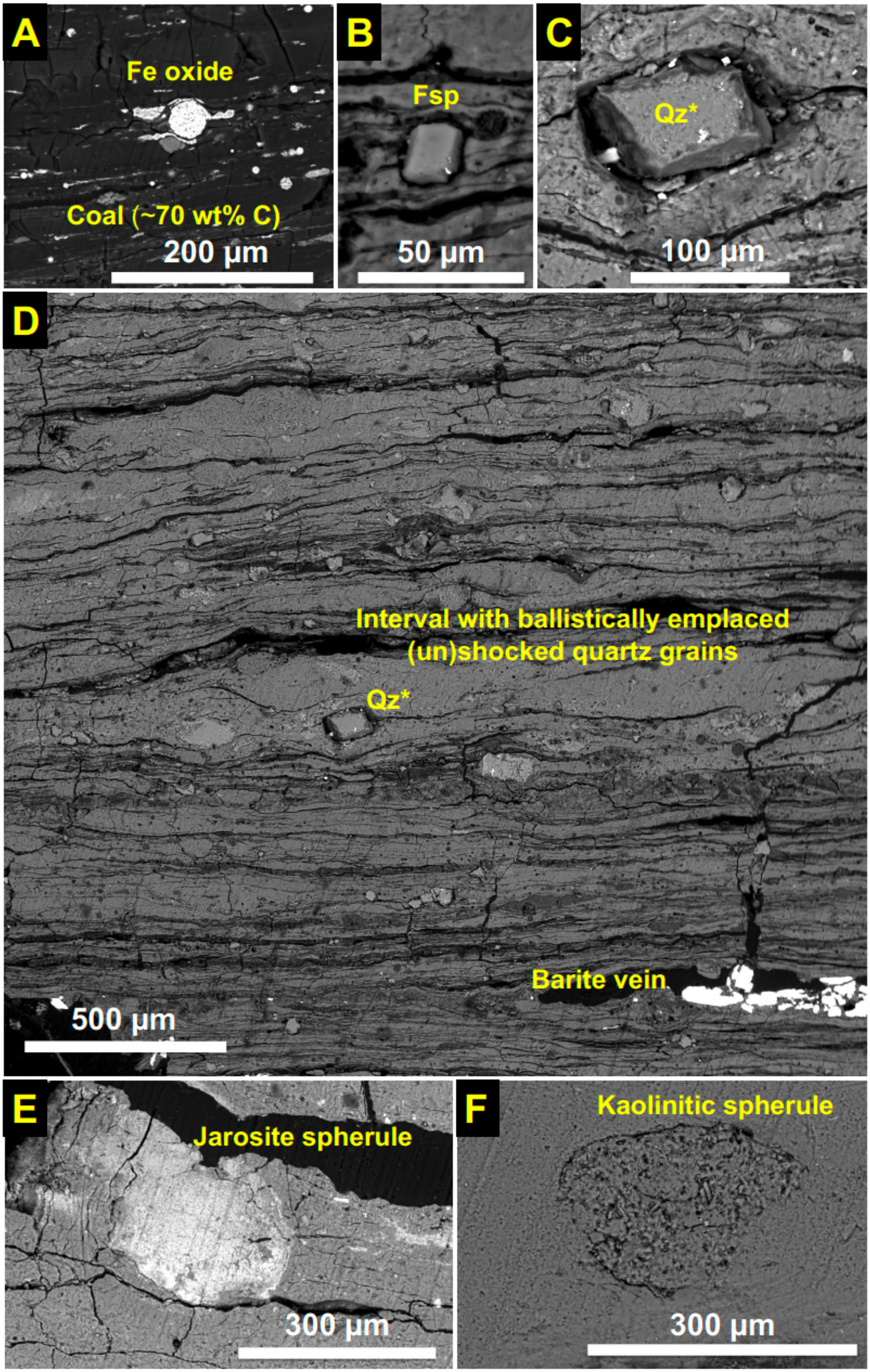
A
Fe oxide
Coal (~70 wt% C)
200 µm
B
Fsp
50 µm
C
Qz*
100 µm
D
Interval with ballistically emplaced
(un)shocked quartz grains
Qz*
Barite vein
500 µm
E
Jarosite spherule
300 µm
F
Kaolinitic spherule
300 µm

315

Figure 3. Representative backscattered electron (BSE) images of impact ejecta components. (A) Lignite matrix with iron oxide. (B) Ejected feldspar from L2. (C) Ejected quartz grain in L2 showing downwarping of surrounding sediment layers indicating ballistic deposition in soft sediment. (D) Overview of sublayer L2 showing ejected quartz minerals with downwarping strata and a barite vein, the latter likely represents authigenic mineralization during peat formation (Rudmin et al., 2018). (E) Jarosite impact spherule in the top part of sublayer L1. (F) Kaolinitic spherule from lower part of L1. The positions of the BSE images are indicated on the slab photo from Fig. 2 with the four sublayers. Mineral abbreviations based on Whitney and Evans, 2010).

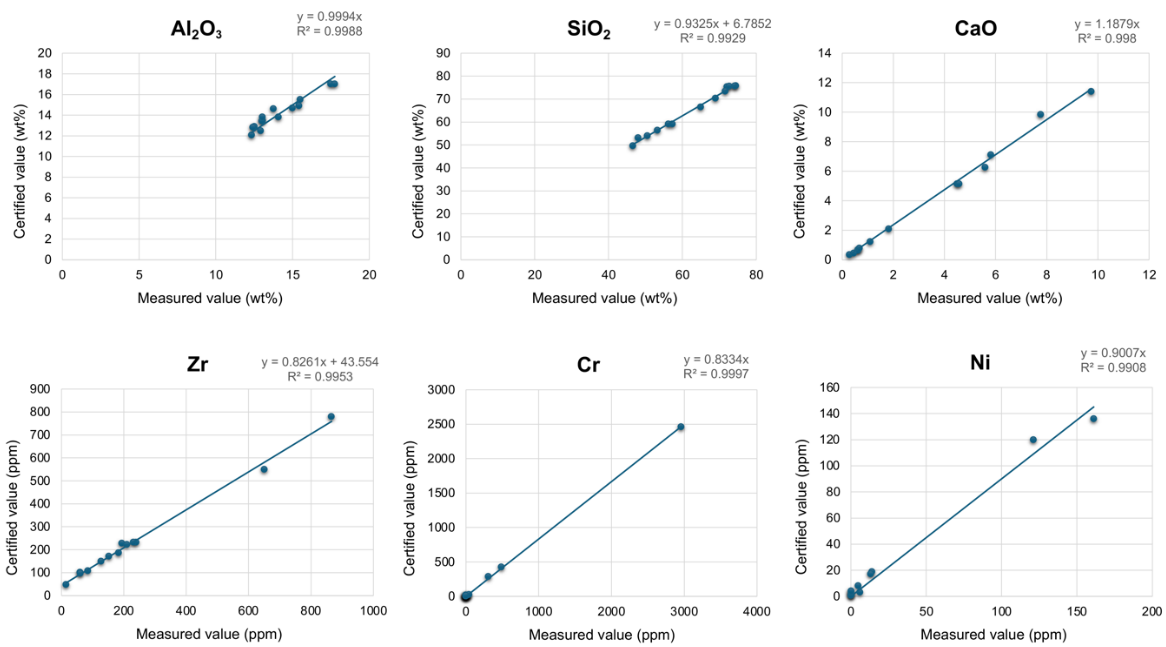

Figure 4. Calibrations using µ-XRF spot analyses on certified reference materials. Representative calibration curves using the mass concentrations exported from the M4 Bruker software and reference values for the major oxides Al_2O_3, SiO_2, CaO, and trace elements Zr, Cr, and Ni. All calibration curves are displayed in Supplementary Figure 2 and the linear regression slope (and possible intercept) with associated coefficients of determination (R^2) are shown in Table 2.

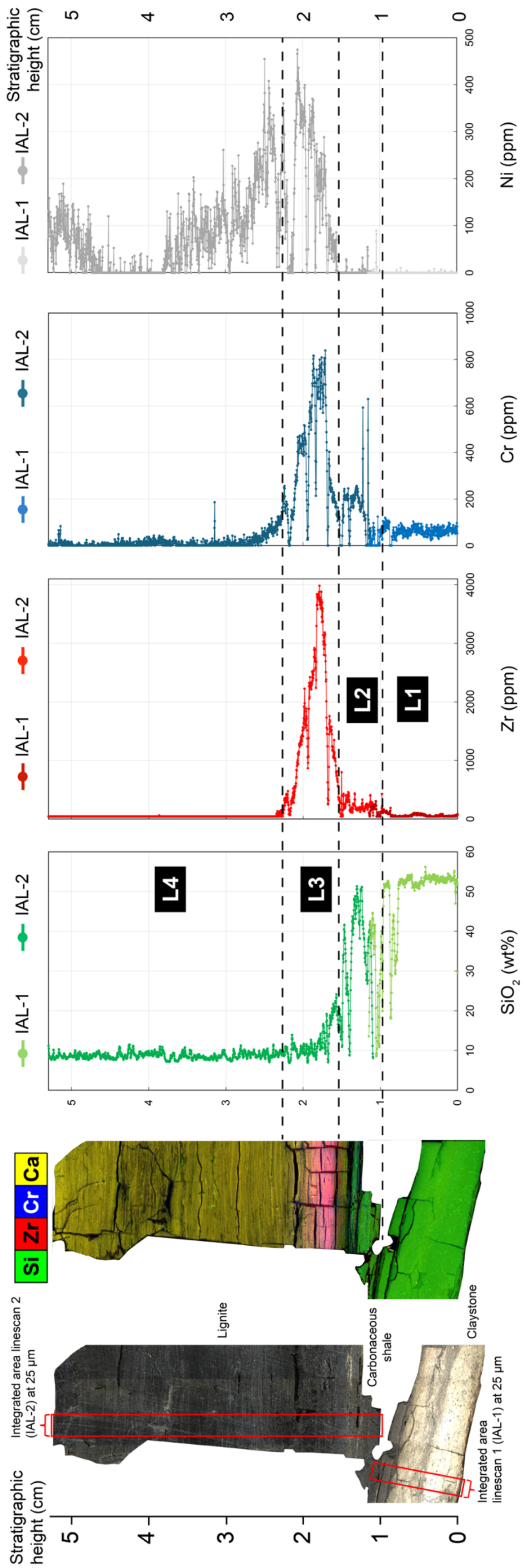
Stratigraphic height (cm)
Integrated area linescan 2 (IAL-2) at 25 µm
Integrated area linescan 1 (IAL-1) at 25 µm
Lignite
Carbonaceous shale
Claystone
Si
Zr
Cr
Ca
IAL-1
IAL-2
SiO2 (wt%)
Zr (ppm)
Cr (ppm)
Ni (ppm)
L1
L2
L3
L4

Figure 5. Overview of quantitative high-resolution (25 µm) µ-XRF linescans of the SVS K-Pg boundary interval. Chemical profiles at 25 µm stratigraphic resolution produced using the integrated area linescan option in the Bruker M4 µ-XRF software, showing the vertical variations of SiO_2 (in wt%), Zr, Cr, and Ni (all in ppm). The two red rectangles refer to the two regions of the integrated-area linescans (IAL-1 and IAL-2: see the two colors in the element profiles). The four sublayers (L1-L4), based on geochemistry and petrography, are marked on the profiles.

5 Discussion

5.1 Novel µ-XRF linescan workflow

The µ-XRF calibration curves on a range of nanopowdered press pellets yield excellent regression lines for 22 elements in total ($R^2 > 0.99$, see Table 2), suitable for accurate quantifications. The integrated-area linescan (IAL) quantification reveals to be a successful measurement mode as it provides a representative integration while still preserving a high stratigraphic resolution of 25 µm necessary for detecting subtle changes in depositional processes. This way, with a single µ-XRF element mapping run already reliable chemical profiles can be extracted without the need for additional point-linescans. In this case study, an integrated area of ~3 mm wide is selected (Fig. 5). Using a wider area in this sample is not feasible due to the presence of cracks filled up by epoxy, resulting in a combined acquisition time of 6 seconds per stratigraphic slice of 25 µm at a measurement time of 50 ms per pixel.

To identify the intervals that might have been chemically affected by the presence of a (micro)crack filled with epoxy, the presence of chlorine was used as a proxy. There are some peaks present in Cl (> 0.3 wt%) in the chemical profile, but the influence on the overall chemostratigraphic trends in key elements such as Si, Zr, Cr and Ni is relatively limited as it affects only thin intervals of < 300 µm (Fig. S3). Moreover, some of the cracks have been filled with the mineral barite ($BaSO_4$; as verified by ESEM-EDS, see Fig. 3D), but these barite veins are not thicker than 400 µm, so the effect on the general chemical trends are also considered limited (Fig. S3).

The sample selected for this study is also challenging in terms of quantifications as it contains a large organic fraction. The M4 Bruker TORNADO µ-XRF instrument cannot detect C, but EDS spot analyses reveal C concentrations of around 70% by weight in sublayer 3 and 4. Here, a universal method for µ-XRF is developed suitable for a range of lithologies and applied without sum-normalization. K-Pg boundaries are often characterized by abrupt lithological changes, for example from a pure limestone to a claystone in marine settings, and a 'one fits all calibration'-approach suitable for a range of matrix compositions is most likely the optimal solution to produce continuous chemical profiles across lithological boundaries. Previous laser ablation−inductively coupled plasma−mass spectrometry (LA-ICP-MS) analysis on the K-Pg boundary preserved in drill core samples from the Demarara Rise (235 µm spotsize) and Chicxulub crater site (150 µm spotsize) showed that a nugget effect can strongly influence a chemical enrichment in siderophile elements (Berndt et al., 2011; Goderis et al., 2021). By systematically introducing µ-XRF mapping and IAL into this workflow, the negative influence of the nugget effect can be visualized and avoided as much as possible before detailed trace and platinum group element analysis is being carried out, for example relying on LA-ICP-MS.

5.2. Geochemical fingerprinting of impact ejecta phases and intervals

For the identification of impact ejecta phases, SiO_2, Zr, Cr, and Ni are selected. K_2O and Al_2O_3 are used to identify different types of clay minerals. Subunit L1 is characterized by a relatively homogeneous composition dominated by SiO_2 (54.2 $\pm$ 3.4 wt%) and Al_2O_3 (36.7 $\pm$ 3.2 wt%), consistent with EDS spot analyses (Fig. 3F) and bulk XRF values (54.8 $\pm$ 0.4 wt% SiO_2; 40.6 $\pm$ 0.5 wt% Al_2O_3, comparison is based on an anhydrous sum-normalization) of the same K-Pg boundary claystone at Starkville-South from Izett (1990). This corresponds to a mineralogy almost exclusively dominated by kaolinite ($Al_2Si_2O_5(OH)_4$), as also evidenced by bulk powder X-ray diffraction (XRD) data from Pollastro & Pillmore (1987).

The overlying subunit L2 shows more chemical variations with a generally lower and more variable SiO_2 content (47.9 $\pm$ 11.9 wt%), lower Al_2O_3 concentrations (24.2 $\pm$ 7.9 wt%), but higher K_2O values (1.8 $\pm$ 0.6 wt% for L2) compared to L1 (0.8 $\pm$ 0.2 wt% K_2O for L1). Pollastro & Pillmore (1987) observed that the shale beds found throughout the K-Pg boundary interval in the Raton Basin consist of a suite of minerals typical of shale, including quartz (20-40 wt%), feldspar, illite-smectite clays, mica (usually illite), and kaolinite. This mineral assemblage explains the more variable composition and the incorporation of K in the presence of the mineral phases K-feldspar ($KAlSi_3O_8$) and illite ($(K,H_3O)(Al,Mg,Fe)_2(Si,Al)_4O_{10}[(OH)_2,(H_2O)]$).

The L2 subunit contains evidence of ejected quartz and feldspar grains based on µ-XRF and ESEM-EDS analyses. Hotspots of zirconium on the high-resolution µ-XRF maps of the scanned epoxy slab likely also reveal the presence of ejected zircon. However, an ESEM-EDS study did not confirm the presence of zircon yet, which could be explained by the attenuation depth of Zr for X-rays (i.e., 0.2-1.1 mm as shown in Kaskes et al., 2021) and hence the presence of a potential zircon grain below the sample surface. More sample material, thin sections and a more detailed petrographic investigation are needed to identify these zircons throughout their microstratigraphy to use them for example for U-Pb dating relying on depth-profiling LA-ICP-MS (Rasmussen et al., 2019) or to characterize their shock state using Electron Backscatter Diffraction (EBSD) (Cavosie et al., 2018).

Subunit L3, on top of the spherule (L1) and ejected quartz bed (L2), represents the transition zone between a carbonaceous shale and lignite. L3 is strongly enriched in Zr, Cr, and Ni. The enrichment in Zr is interpreted to be linked to the presence of ultrafine dust composed of pulverized Yucatán granitic basement. Based on previous geochemical analyses on K-Pg boundaries (de la Parra et al., 2022) and impactites from the Chicxulub crater (Goderis et al., 2021; Feignon et al., 2022), Cr and Ni have successfully been used as a marker for meteoritic contribution as these siderophile elements behave chemically similarly to platinum group elements such as iridium (Schmitz, 1992; Goderis et al., 2013).

Unit L4 consists purely of a lignite with an estimated carbon content value of 70 wt%. The remaining inorganic matter in the lignite shows relatively low values of SiO_2 (2.1 ± 0.9 wt% after recalculation based on 30 wt% mineral fraction) and Al_2O_3 (1.4 ± 0.6 wt%), but higher concentrations in CaO (3.2 ± 1.3 wt%), and Fe_2O_3 (19.8 ± 3.4 wt%). A similar trend with relatively high CaO and Fe_2O_3 concentration values is found in the Neogene Velenje lignite in Slovenia (Markič, 2006), showing that these elements are mostly organically bound. The Velenje lignite corresponds to a fine detrital coal, interpreted to be deposited at a swamp-lake border closer to open water settings, which might also be the case for the SVS lignite (Markič, 2006).

5.3. Impact ejecta chronology and emplacement mechanisms

Figure 6 summarizes the chronology and emplacement mechanisms of the Chicxulub impact ejecta sequence. The Starkville K-Pg impact ejecta sequence started with the deposition of (now replaced) glassy impact spherules (microtektites), which have been detected as ~300 µm sized homogeneous, spherulitic objects in the basal claystone. These spherules subsequently altered to kaolinite, goyazite, or jarosite in the acidic reducing environment of the coal swamps, and now form the thick kaolinitic boundary claystone (L1) (Izett, 1990; Pillmore et al., 1984; Pollastro & Pillmore, 1987). These formerly glassy melt spherules are interpreted to have formed by near-instantaneous shock-melting (Belza et al., 2015) and launched in a turbulent ejecta curtain with angles of 30-45° relative to the surface outside the crater (Alvarez et al., 1995), followed by rapid quenching in flight during the ballistic transport to the place of deposition. The latter likely occurred for US Western Interior sites within ~10-15 minutes (Fig. 6; Alvarez et al., 1995; Artemieva & Morgan, 2020).

The overlying carbonaceous shale layer (L2) consists of multiple ejected quartz and feldspar grains that are thought to have been ballistically expelled out of the crater as part of the 'warm 'fireball phase' with a trajectory most likely steeper than ~65°. Compared to the microtektites, this would result in a slighter slower deposition rate in the order of ~20 minutes to 2 hours, depending on the size of the minerals, the launch angle and the final site of deposition (Fig. 6) (Alvarez et al., 1995; Kring and Durda, 2002). This layer is known as the 'fireball layer'. Chronometric dating using U-Pb of highly shocked zircons from this layer in the Raton Basin of Colorado have revealed resetting ages around ~66 Ma, consistent with their association to the Chicxulub impact structure (Krogh et al., 1993b)

Alvarez et al. (1995) proposed that the iridium, as part of an extremely hot fireball consisting of vaporized meteorite and target rock carbonate and silicate, likely deposited as a separate veneer on top of the ejected quartz layer. This proposed 'third layer' has likely been identified in this study using µ-XRF at the Starkville K-Pg site on the basis of a transitional interval (L3) between a carbonaceous shale and a lignite that is enriched in Zr, Cr, and Ni. This coaly interval is characterized by the highest Zr concentrations of the identified intervals (up to 4725 ppm; Fig. 5), which is interpreted here as being related to a pulverized fraction of the unmelted felsic crystalline basement incorporated within the impact dust plume. Geochemical analyses of granitoids from the recent IODP-ICDP Expedition 364 drilling within the Chicxulub peak ring have shown average Zr values of ~100 ppm (Feignon et al., 2021). The enriched Zr values in L3 are most probably related to the refractory behavior and high condensation temperature of Zr (T_{50} of 1722 K (Wood et al., 2019)) within the impact dust plume (Belza et al., 2017), likely steering its slow atmospheric deposition.

The bulge with high Zr values (> 2500 ppm) from Starkville, between ~1.7-1.9 cm stratigraphic height, corresponds also to a broad peak in high Cr values (> 600 ppm) (Fig. 5). These high Cr values in the coaly interval (L3) most likely correspond to the Ir and PGE anomaly, as can also be deduced from a similar linear relationship between these two elements as found in the Chicxulub crater itself (Goderis et al., 2021) and other terrestrial and marine K-Pg boundaries around the world (Schmitz, 1992; Goderis et al., 2013; Feignon et al., 2022). The highest Ir values for Starkville described in literature are found in the shocked mineral-bearing carbonaceous shale (“fireball layer”: ~56 ppb; Pillmore et al., 1984) or from the interval between this layer and the lignite above (~16 ppb; Tschudy et al., 1984; Fig. 1E). In this study, this corresponds to L2 and the transition between L2 to L3, whereas the highest Cr values in this study are found in L3. Elevated Ir values have been found in a coaly interval above the K-Pg boundary claystone at the site of Madrid East and Clear Creek North based on previous low-resolution studies with up to 10.9 and 14.6 ppb Ir, respectively (Izett, 1990). However, these bulk powder-based studies are relatively low-resolution and future work should focus on more high-resolution PGE datasets. Considering a direct relationship between Cr and Ir, this would mean that the return to background values for Cr marks the final atmospheric settling of fine meteoritic and granitic dust, which has been estimated to have taken less than 20 years post-impact based on atmospheric modelling (Kring and Durda, 2002; Goderis et al., 2021; Senel et al., 2023). Also, peaks of Ni and Cr on the µ-XRF maps might hint to the possible presence of microkrystites containing Ni-Cr-rich and Mg-poor spinel group minerals (Smit, 1999; Kyte & Smit, 1986). So far, these microkrystites have petrographically not been verified during the ESEM-EDS survey, but their presence has been recorded from the uppermost claystone bed from the Tanis K-Pg site (DePalma et al., 2019). An in-depth petrographic analysis on more material from the Raton Basin is preferred to confirm or deny the presence of microkrystites. The highest Ni values in L3 (> 300 ppm) are seen stratigraphically slightly higher (~1.85-2.09 cm height) compared to Zr and Cr (~1.7-1.9 cm) and this upward shift might be related to Ni remobilization in the organic rich environment.

This pattern for Ni is also seen in the overlying L4. This sublayer still displays high values of Ni (up to 455 ppm), compared to very low Zr (>50 ppm) and low Cr values (>200 ppm). Ni is more mobile than Cr and Zr (Agnieszka and Barbara, 2012) and therefore likely explains such a contrasting profile. L4 becomes more depleted in Al_2O_3 and SiO_2 upwards and more CaO rich (Fig. S3), suggesting that the lignite become more organic rich with a smaller influence of detrital input towards the top in a paludal/lacustrine paleoenvironment. This lignite is approximately 5 cm thick throughout the Raton Basin and shows the presence of a fern spike:

an anomalous abundance of fossil fern spores relative to other palynoflora in the aftermath of the Chicxulub impact (Tschudy et al., 1984). The duration of this period of fern dominance in the earliest Danian has been estimated to have lasted for (several) millennia (kyr) (Berry, 2019). This age indication likely marks the upper boundary of the Ni remobilization. However, more detailed work on fine-grained ejecta components in the lignite, in conjunction with ejecta modelling and high-resolution palynology provide more constraints on this timeframe. Generally, applying a similar µ-XRF-IAL method on other K-Pg boundaries in the Raton Basin and beyond may constrain potential post-impact alteration in more detail with the aim to further disentangle the complex ejecta dynamics related to the Chicxulub impact event.

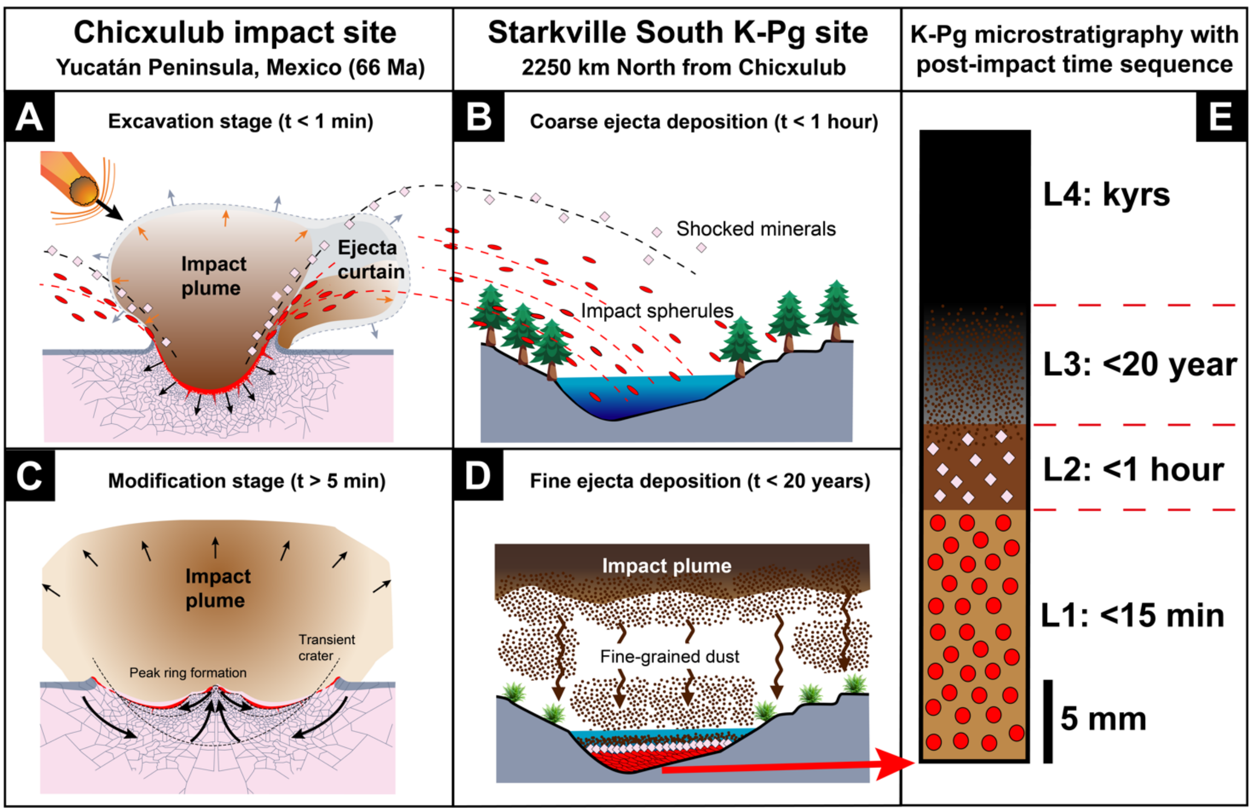

Figure 6. Schematic visualization of key time intervals in the emplacement of Chicxulub impact ejecta and an idealized K-Pg microstratigraphy of the Raton Basin. This simplified model (not to scale, based on Pierazzo and Artemieva, 2012; Belza, 2015; Collins et al., 2020) displays the results of an 45° oblique impact from the NE. The Yucatán target stratigraphy and the different types of coarse impact ejecta (glassy impact melt spherules and shocked minerals derived from the granitic basement) and fine-grained impact ejecta (including silicate dust) are highlighted with their interpreted timing post-impact (Artemieva & Morgan, 2020; Alvarez et al., 1995; Goderis et al., 2021, Senel et al., 2023). A) Excavation stage at the Chicxulub crater region showing the initiation of the ejecta curtain (< 1 minute post-impact). B) Coarse-grained ejecta deposition at the Starkville-South K-Pg boundary site showing first the deposition of impact spherules (< 15 minutes) followed by the ballistic emplacement of (shocked) basement

mineral grains. C) The modification stage in the crater region showing peak ring formation and the rise of the impact plume into the stratosphere (> 5 minutes). D) Fine-grained ejecta deposition at the Starkville-South K-Pg boundary site derived from an impact dust plume rich in pulverized granitic material and an admixed meteoritic component (< 20 years after impact). E) An idealized K-Pg microstratigraphy of the Raton Basin showing the interpreted chronology displaying a kaolinitic claystone interval with glassy impact spherules (L1), followed by a carbonaceous shale interval with shocked minerals (L2), which is capped by a coaly interval enriched in fine Zr and Cr rich dust (L3), that transitions into a lignite without major atmospheric dust input (L4).

6 Conclusions

The µ-XRF workflow approach developed in this study generates high-resolution chemostratigraphic records of key stratigraphic intervals. This is exemplified here with a continuous sediment slab from a terrestrial Cretaceous-Paleogene (K-Pg) boundary. This workflow is powerful in geochemically fingerprinting specific impact ejecta products and thereby elucidating the timeline of the complex ejecta processes involved. High-resolution µ-XRF mapping and quantitative linescans (25 µm) in combination with ESEM-EDS petrography revealed that the Starkville South sequence has a more complex microstratigraphy than the 'dual-layer' succession described in literature for US Western Interior K-Pg sites. In this study, the sample stratigraphy encompasses four layers (L1 – L4). First, a basal claystone is identified with abundant glassy impact spherules that have now been altered to kaolinite and jarosite (L1), due to the acidic and reducing conditions in a local swamp environment. This first lithology is followed by a carbonaceous shale interval rich in ejected quartz grains (L2). Using ESEM-EDS analyses, these two ejecta intervals, which are interpreted to have formed by ballistic transport from the Chicxulub crater region and were likely emplaced within ~1 hour after impact at Starkville. Subsequently, pronounced enrichments in both zirconium and chromium are detected in the overlying lignite layer (L3), which are attributed to fine-grained impact dust comprising pulverized granitoid basement with admixture of meteoritic material, likely deposited <20 years after impact through slow atmospheric settling. Based on the previously observed linear relationship between chromium and iridium, this suggests that a large part of the iridium-rich particles settled during the deposition of the basal part of the coaly layer instead of during the underlying 'fireball layer'. Based on low zirconium contents, a final interval in the lignite layer (L4) is identified, which is still enriched in nickel likely linked to post-impact mobilization in a detrital coal swamp environment during the millennia post-impact. These geochemical observations can serve as input parameters for ejecta models, which can shed more light on the timing and mechanisms of impact ejecta processes for Chicxulub and other impact events in the Solar System.

As Applicable – Inclusion in Global Research Statement

The Authorship: Inclusion in Global Research policy aims to promote greater equity and transparency in research collaborations. AGU Publications encourage research collaborations between regions, countries, and communities and expect authors to include their local collaborators as co-authors when they meet the AGU Publications authorship criteria. Those who do not meet the criteria should be included in the Acknowledgement section. We encourage researchers to consider recommendations from The TRUST CODE - A Global Code of Conduct for Equitable Research Partnerships when conducting and reporting their research, as applicable, and encourage authors to include a disclosure statement pertaining to the ethical and scientific considerations of their research collaborations in an “**Inclusion in Global Research Statement’** as a standalone section in the manuscript following the Conclusions section. This can include disclosure of permits, authorizations, permissions and/or any formal agreements with local communities or other authorities, additional acknowledgements of local help received, and/or description of end-users of the research. You can learn more about the policy in this editorial. Example statements can be found in the following published papers: Holt et al., Sánchez-Gutiérrez et al., Tully et al. Please note that these statements are titled as “Global Research Collaboration Statements” from a previous pilot requirement in *JGR Biogeosciences*. The pilot has ended and statements should now be titled “Inclusion in Global Research Statement”.

Acknowledgments

This research is financially supported by the Barringer Family Fund for Meteorite Impact Research 2019 awarded to Pim Kaskes, the Belgian Federal Science Policy (BELSPO) project Chicxulub and the Research Foundation - Flanders (FWO) projects G0A6517N to Philippe Claeys and 11E6621N (PhD Fellowship awarded to Pim Kaskes). Philippe Claeys and Steven Goderis thank the Excellence of Science project “ET-HoME” for support and the FWO - Hercules Program for financing the µ-XRF instrument at the VUB. We thank Jana Bergholz for information on the field and lab procedures and the photo in Fig. 1E. My-standards (GMBH, Germany) is thanked for the usage of the nano-powders.

Open Research

All µ-XRF data from this study is available via the Zenodo online repository: https://zenodo.org/records/14552419.

References

Agnieszka, J., and Barbara, G., 2012, Chromium, nickel and vanadium mobility in soils derived from fluvioglacial sands: Journal of hazardous materials, v. 237, p. 315–322.

Alvarez, L.W., Alvarez, W., Asaro, F., and Michel, H. V., 1980, Extraterrestrial cause for the Cretaceous-Tertiary extinction: Science, v. 208, no. 4448, p. 1095–1108, doi: 10.1126/science.208.4448.1095.

Alvarez, W., Claeys, P., and Kieffer, S.W., 1995, Emplacement of Cretaceous-Tertiary boundary shocked quartz from Chicxulub crater: Science, v. 269, no. 5226, p. 930–935, doi: 10.1126/science.269.5226.930.

Artemieva, N., and Morgan, J., 2020, Global K-Pg Layer Deposited From a Dust Cloud: Geophysical Research Letters, v. 47, no. 6, p. 1–8, doi: 10.1029/2019GL086562.

Artemieva, N., and Morgan, J., 2009, Modeling the formation of the K-Pg boundary layer: Icarus, v. 201, no. 2, p. 768–780, doi: 10.1016/j.icarus.2009.01.021.

Arz, J.A., Arenillas, I., Grajales-Nishimura, J.M., Liesa, C.L., Soria, A.R., Rojas, R., Calmus, T., and Gilabert, V., 2022, No evidence of multiple impact scenario across the Cretaceous/Paleogene boundary based on planktic foraminiferal biochronology: Special Paper of the Geological Society of America, v. 557, no. 20, p. 415–448, doi: 10.1130/2022.2557(20).

Belza, J., 2015, Petrography and geochemistry of ejecta material from the K-Pg boundary Chicxulub crater (Yucatan, Mexico): PhD Thesis - Vrije Universiteit Brussel /Universiteit Gent, p. 361.

Belza, J., Goderis, S., Montanari, A., Vanhaecke, F., and Claeys, P., 2017, Petrography and geochemistry of distal spherules from the K–Pg boundary in the Umbria–Marche region (Italy) and their origin as fractional condensates and melts in the Chicxulub impact plume: Geochimica et Cosmochimica Acta, v. 202, no. January, p. 231–263, doi: 10.1016/j.gca.2016.12.018.

Belza, J., Goderis, S., Smit, J., Vanhaecke, F., Baert, K., Terryn, H., and Claeys, P., 2015, High spatial resolution geochemistry and textural characteristics of “microtektite” glass spherules in proximal Cretaceous-Paleogene sections: Insights into glass alteration patterns and precursor melt lithologies: Geochimica et Cosmochimica Acta, v. 152, p. 1–38, doi: 10.1016/j.gca.2014.12.013.

Berlin, J., Cohen, B.A., Newsom, H.E., and Tagle, R., 2010, Another Anniversary: 5 Years Since the K/P Boundary Sample Started its Journey from Starkville/Colorado to the Riescrater-Museum in Nördlingen: Nördlingen 2010: The Ries Crater, the Moon, and the Future of Human Space Exploration, v. 1559, p. 4.

Berndt, J., Deutsch, A., Schulte, P., and Mezger, K., 2011, The Chicxulub ejecta deposit at Demerara Rise (western Atlantic): Dissecting the geochemical anomaly using laser ablation–mass spectrometry: Geology, v. 39, no. 3, p. 279–282, doi: 10.1130/G31599.1.

Berry, K., 2019, Fern spore viability considered in relation to the duration of the Cretaceous-Paleogene (K-Pg) impact winter. A contribution to the discussion: Acta Palaeobotanica, v. 59, no. 1, p. 19–25, doi: 10.2478/acpa-2019-0008.

Boer, W., Nordstad, S., Weber, M., Mertz-Kraus, R., Hönisch, B., Bijma, J., Raitzsch, M., Wilhelms-Dick, D., Foster, G.L., Goring-Harford, H., Nürnberg, D., Hauff, F., Kuhnert, H., Lugli, F., et al., 2022, New Calcium Carbonate Nano-particulate Pressed Powder Pellet (NFHS-2-NP) for LA-ICP-OES, LA-(MC)-ICP-MS and µXRF: Geostandards and Geoanalytical Research, v. 46, no. 3, p. 411–432, doi: 10.1111/ggr.12425.

Bohor, B.F., Betterton, W.J., and Krogh, T.E., 1993, Impact-shocked zircons: discovery of shock-induced textures reflecting increasing degrees of shock metamorphism: Earth and Planetary Science Letters, v. 119, no. 3, p. 419–424.

Bohor, B.F., Foord, E.E., Modreski, P.J., and Triplehorn, D.M., 1984, Mineralogic evidence for an impact event at the Cretaceous-Tertiary boundary: Science, v. 224, no. 4651, p. 867–869.

Bohor, B.F., Modreski, P.J., and Foord, E.E., 1987, Shocked quartz in the Cretaceous-Tertiary boundary clays: Evidence for a global distribution: Science, v. 236, no. 4802, p. 705–709.

Cavosie, A.J., Timms, N.E., Ferrière, L., and Rochette, P., 2018, FRIGN zircon—The only terrestrial mineral diagnostic of high-pressure and high-temperature shock deformation: Geology, v. 46, no. 10, p. 891–894.

Claeys, P., Kiessling, W., and Alvarez, W., 2002, Distribution of Chicxulub ejecta at the Cretaceous-Tertiary boundary: Special Paper of the Geological Society of America, v. 356, p. 55–68, doi: 10.1130/0-8137-2356-6.55.

Collins, G.S., Patel, N., Davison, T.M., Rae, A.S.P., Morgan, J. V., Gulick, S.P.S., Christeson, G.L., Chenot, E., Claeys, P., Cockell, C.S., Coolen, M.J.L., Ferrière, L., Gebhardt, C., Goto, K., et al., 2020, A steeply-inclined trajectory for the Chicxulub impact: Nature Communications, v. 11, no. 1, p. 1–10, doi: 10.1038/s41467-020-15269-x.

Decrée, S., Cawthorn, G., Deloule, E., Mercadier, J., Frimmel, H., and Baele, J.-M., 2020, Unravelling the processes controlling apatite formation in the Phalaborwa Complex (South

Africa) based on combined cathodoluminescence, LA-ICPMS and in-situ O and Sr isotope analyses: Contributions to Mineralogy and Petrology, v. 175, p. 1–31.

DePalma, R.A., Smit, J., Burnham, D.A., Kuiper, K., Manning, P.L., Oleinik, A., Larson, P., Maurrasse, F.J., Vellekoop, J., Richards, M.A., Gurche, L., and Alvarez, W., 2019, A seismically induced onshore surge deposit at the KPg boundary, North Dakota: Proceedings of the National Academy of Sciences of the United States of America, doi: 10.1073/pnas.1817407116.

Feignon, J., Ferrière, L., Leroux, H., and Koeberl, C., 2020, Characterization of shocked quartz grains from Chicxulub peak ring granites and shock pressure estimates: Meteoritics and Planetary Science, v. 55, p. 2206–2223, doi: 10.1111/maps.13570.

Feignon, J.-G., de Graaff, S.J., Ferrière, L., Kaskes, P., Déhais, T., Goderis, S., Claeys, P., and Koeberl, C., 2021, Chicxulub impact structure, IODP-ICDP Expedition 364 drill core: geochemistry of the granite basement: Meteoritics & Planetary Science, v. 56, no. 7, p. 1243–1273, doi: https://doi.org/10.1111/maps.13705.

Feignon, J.-G., Schulz, T., Ferrière, L., Goderis, S., de Graaff, S.J., Kaskes, P., Déhais, T., Claeys, P., and Koeberl, C., 2022, Search for a meteoritic component within the impact melt rocks of the Chicxulub impact structure peak ring, Mexico: Geochimica et Cosmochimica Acta, v. 323, p. 74–101, doi: https://doi.org/10.1016/j.gca.2022.02.006.

Goderis, S., Sato, H., Ferrière, L., Schmitz, B., Burney, D., Kaskes, P., Vellekoop, J., Wittmann, A., Schulz, T., Chernonozhkin, S.M., Claeys, P., de Graaff, S.J., Déhais, T., de Winter, N.J., et al., 2021, Globally distributed iridium layer preserved within the Chicxulub impact structure: Science Advances, v. 7, no. 9, p. eabe3647, doi: 10.1126/sciadv.abe3647.

Goderis, S., Tagle, R., Belza, J., Smit, J., Montanari, A., Vanhaecke, F., Erzinger, J., and Claeys, P., 2013, Reevaluation of siderophile element abundances and ratios across the Cretaceous-Paleogene (K-Pg) boundary: Implications for the nature of the projectile: Geochimica et Cosmochimica Acta, v. 120, p. 417–446, doi: 10.1016/j.gca.2013.06.010.

de Graaff, S.J., Kaskes, P., Déhais, T., Goderis, S., Debaille, V., Ross, C.H., Gulick, S.P.S., Feignon, J.-G., Ferrière, L., Koeberl, C., Smit, J., Mattielli, N., and Claeys, P., 2022, New insights into the formation and emplacement of impact melt rocks within the Chicxulub impact structure, following the 2016 IODP-ICDP Expedition 364: GSA Bulletin, v. 134, no. 1–2, p. 293–315, doi: 10.1130/B35795.1.

Gulick, S.P.S., Bralower, T.J., Ormö, J., Hall, B., Grice, K., Schaefer, B., Lyons, S., Freeman, K.H., Morgan, J. V., Artemieva, N., Kaskes, P., De Graaff, S.J., Whalen, M.T., Collins, G.S., et al., 2019, The first day of the Cenozoic: Proceedings of the National Academy of Sciences of the United States of America, v. 116, no. 39, p. 19342–19351, doi: 10.1073/pnas.1909479116.

Hildebrand, A.R., Penfield, G.T., Kring, D.A., Pilkington, M., Camargo Z., A., Jacobsen, S.B., and Boynton, W. V., 1991, Chicxulub crater - a possible Cretaceous/Tertiary boundary impact crater on the Yucatan Peninsula, Mexico: Geology, v. 19, no. 9, p. 867–871, doi: 10.1130/0091-7613(1991)019<0867.

Hoffman, G.K., and Jopnes, G.E., 2005, Availability of Coal Resources in the Vermejo and Raton formations, Raton coalfield, Raton Basin, northeast New Mexico:

Izett, G.A., 1990, The Cretaceous/Tertiary boundary interval, Raton Basin, Colorado and New Mexico, and its content of shock-metamorphosed minerals; evidence relevant to the K/T boundary impact-extinction theory: GSA Special Paper, v. 249, p. 100.

Jochum, K.P., Nohl, U., Herwig, K., Lammel, E., Stoll, B., and Hofmann, A.W., 2005, GeoReM: A new geochemical database for reference materials and isotopic standards: Geostandards and Geoanalytical Research, v. 29, no. 3, p. 333–338, doi: 10.1111/j.1751-908x.2005.tb00904.x.

Kamo, S.L., and Krogh, T.E., 1995, Chicxulub crater source for shocked zircon crystals from the Cretaceous-Tertiary boundary layer, Saskatchewan: evidence from new U-Pb data: Geology, v. 23, no. 3, p. 281–284, doi: 10.1130/0091-7613(1995)023<0281:CCSFSZ>2.3.CO;2.

Kaskes, P., Déhais, T., de Graaff, S.J., Goderis, S., and Claeys, P., 2021, Micro–X-ray fluorescence (µXRF) analysis of proximal impactites: High-resolution element mapping, digital image analysis, and quantifications (W. U. Reimold & C. Koeberl, Eds.): Geological Society of America Special Paper, v. 550, p. 171–206, doi: 10.1130/2021.2550(07).

Kaskes, P., de Graaff, S.J., Feignon, J.-G., Déhais, T., Goderis, S., Ferrière, L., Koeberl, C., Smit, J., Wittmann, A., Gulick, S.P.S., Debaille, V., Mattielli, N., and Claeys, P., 2022, Formation of the crater suevite sequence from the Chicxulub peak ring: A petrographic, geochemical, and sedimentological characterization: Bulletin of the Geological Society of America, v. 134, no. 3–4, p. 895–927, doi: 10.1130/B36020.1.

Kaskes, P., Marchegiano, M., Peral, M., Goderis, S., and Claeys, P., 2024, Hot carbonates deep within the Chicxulub impact structure: PNAS Nexus, v. 3, no. 1, p. pgad414, doi: 10.1093/pnasnexus/pgad414.

Kring, D.A., 2007, The Chicxulub impact event and its environmental consequences at the

Cretaceous-Tertiary boundary: Palaeogeography, Palaeoclimatology, Palaeoecology, v. 255, no. 1–2, p. 4–21, doi: 10.1016/j.palaeo.2007.02.037.

Kring, D.A., and Boynton, W. V., 1992, Petrogenesis of an augite-bearing melt rock in the Chicxulub structure and its relationship to K/T impact spherules in Haiti: Nature, v. 358, no. 6382, p. 141–144, doi: 10.1038/358141a0.

Kring, D.A., Claeys, P., Gulick, S.P.S., Morgan, J. V., Collins, G.S., Bralower, T., Chenot, E., Christeson, G., Cockell, C., Coolen, M.J.L., Ferrière, L., Gebhardt, C., Goto, K., Jones, H., et al., 2017, Chicxulub and the exploration of large peak-ring impact craters through scientific drilling: GSA Today, v. 27, no. 10, p. 4–8, doi: 10.1130/GSATG352A.1.

Kring, D.A., and Durda, D.D., 2002, Trajectories and distribution of material ejected from the Chicxulub impact crater: Implications for postimpact wildfires: Journal of Geophysical Research E: Planets, v. 107, no. 8, doi: 10.1029/2001je001532.

Krogh, T.E., Kamo, S.L., and Bohor a, B.F., 1993a, Fingerprinting the K/T impact site and determining the time of impact by UPb dating of single shocked zircons from distal ejecta: Earth and Planetary Science Letters, v. 119, no. 3, p. 425–429.

Krogh, T.E., Kamo, S.L., Sharpton, V.L., Marin, L.E., and Hildebrands, A.R., 1993b, U–Pb ages of single shocked zircons linking distal K/T ejecta to the Chicxulub crater: Nature, v. 366, no. 6457, p. 731–734, doi: 10.1038/366731a0.

de la Parra, F., Jaramillo, C., Kaskes, P., Goderis, S., Claeys, P., Villasante-Marcos, V., Bayona, G., Hatsukawa, Y., and Caballero, D., 2022, Unraveling the record of a tropical continental Cretaceous-Paleogene boundary in northern Colombia, South America: Journal of South American Earth Sciences, v. 114, p. 103717.

Markič, M., 2006, Inorganic geochemical characterisation of the Velenje lignite in the representative P-9k/92 borehole profile (Slovenia): Geologija, v. 49, no. 2, p. 311–338.

Morgan, J. V., Bralower, T.J., Brugger, J., and Wünnemann, K., 2022, The Chicxulub impact and its environmental consequences: Nature Reviews Earth and Environment, v. 3, no. 5, p. 338–354, doi: 10.1038/s43017-022-00283-y.

Orth, C.J., Gilmore, J.S., Knight, J.D., Pillmore, C.L., Tschudy, R.H., and Fassett, J.E., 1981, An Iridium Abundance Anomaly at the Palynological Cretaceous-Tertiary Boundary in Northern New Mexico: Science, v. 214, no. 4527, p. 1341–1343, doi: 10.1126/science.214.4527.1341.

Pierazzo, E., and Artemieva, N., 2012, Local and global environmental effects of impacts on earth: Elements, v. 8, no. 1, p. 55–60, doi: 10.2113/gselements.8.1.55.

Pillmore, C.L., and Flores, R.M., 1987, Stratigraphy and depositional environments of the Cretaceous-Tertiary boundary clay and associated rocks: Raton Basin, New Mexico and Colorado: GSA Special Paper, v. 209, p. 111–130.

Pillmore, C.L., Tschudy, R.H., Orth, C.J., Gilmore, J.S., and Knight, J.D., 1984, Geologic framework of nonmarine Cretaceous- Tertiary boundary sites, Raton Basin, New Mexico and Colorado.: Science, v. 223, no. 4641, p. 1180–1183, doi: 10.1126/science.223.4641.1180.

Pollastro, R.M., and Pillmore, C.L., 1987, Mineralogy and petrology of the Cretaceous- Tertiary boundary clay bed and adjacent clay-rich rocks, Raton Basin, New Mexico and Colorado.: Journal of Sedimentary Petrology, v. 57, no. 3, p. 456–466, doi: 10.1306/212F8B61-2B24-11D7-8648000102C1865D.

Rasmussen, C., Stockli, D.F., Ross, C.H., Pickersgill, A., Gulick, S.P., Schmieder, M., Christeson, G.L., Wittmann, A., Kring, D.A., and Morgan, J. V., 2019, U-Pb memory behavior in Chicxulub's peak ring — Applying U-Pb depth profiling to shocked zircon: Chemical Geology, v. 525, no. July, p. 356–367, doi: 10.1016/j.chemgeo.2019.07.029.

Robin, E., Bonté, P., Froget, L., Jéhanno, C., and Rocchia, R., 1992, Formation of spinels in cosmic objects during atmospheric entry: A clue to the Cretaceous-Tertiary boundary event: Earth and Planetary Science Letters, v. 108, no. 4, p. 181–190.

Rousseau, R.M., 1984a, Fundamental algorithm between concentration and intensity in XRF analysis 1—theory: X-Ray Spectrometry, v. 13, no. 3, p. 115–120.

Rousseau, R.M., 1984b, Fundamental algorithm between concentration and intensity in XRF analysis 2—practical application: X-Ray Spectrometry, v. 13, no. 3, p. 121–125.

Rousseau, R.M., and Bouchard, M., 1986, Fundamental algorithm between concentration and intensity in XRF analysis. 3—Experimental verification: X-Ray Spectrometry, v. 15, no. 3, p. 207–215.

Rudmin, M., Ruban, A., Savichev, O., Mazurov, A., Dauletova, A., and Savinova, O., 2018, Authigenic and Detrital Minerals in Peat Environment of Vasyugan Swamp, Western Siberia: Minerals, v. 8, no. 11, doi: 10.3390/min8110500.

Schmitz, B., 1992, Chalcophile elements and Ir in continental Cretaceous-Tertiary boundary clays from the western interior of the USA: Geochimica et Cosmochimica Acta, v. 56, no. 4, p. 1695–1703, doi: https://doi.org/10.1016/0016-7037(92)90235-B.

Schulte, P., Alegret, L., Arenillas, I., Arz, J.A., Barton, P.J., Bown, P.R., Bralower, T.J., Christeson, G.L., Claeys, P., Cockell, C.S., Collins, G.S., Deutsch, A., Goldin, T.J., Goto, K., et al., 2010, The Chicxulub asteroid impact and mass extinction at the Cretaceous-Paleogene boundary:

Science, v. 327, no. 5970, p. 1214–1218.

Schwartz, T.M., Dechesne, M., and Zellman, K.L., 2021, Evidence for variable precipitation and discharge from upper cretaceous-paleogene fluvial deposits of the Raton Basin, Colorado-New Mexico, U.S.A.: Journal of Sedimentary Research, v. 91, no. 6, p. 571–594, doi: 10.2110/jsr.2020.081.

Scotese, C.R., 2004, A continental drift flipbook: The Journal of geology, v. 112, no. 6, p. 729–741.

Senel, C., Kaskes, P., Temel, O., Vellekoop, J., Goderis, S., DePalma, R.A., Prins, M., Claeys, P., and Karatekin, O., 2023, Chicxulub impact winter sustained by fine silicate dust: Nature Geoscience,.

Sharpton, V.L., Schuraytz, B.C., Burke, K., Murali, A. V., and Ryder, G., 1990, Detritus in K/T boundary clays of western North America; Evidence against a single oceanic impact: Special Paper of the Geological Society of America, v. 247, p. 349–357, doi: 10.1130/SPE247-p349.

Sherman, J., 1955, The theoretical derivation of fluorescent X-ray intensities from mixtures: Spectrochimica Acta, v. 7, p. 283–306.

Smit, J., 1999, The global stratigraphy of the Cretaceous-Tertiary boundary impact ejecta: Annual Review of Earth and Planetary Sciences, v. 27, no. 1, p. 75–113, doi: 10.1146/annurev.earth.27.1.75.

Smit, J., Alvarez, W., Montanari, A., Swinburne, N., Van Kempen, T.M., Klaver, G.T., and Lustenhouwer, W.J., 1992a, "Tektites" and microkrystites at the Cretaceous Tertiary boundary-Two strewn fields, one crater?, *in* Proceedings of Lunar and Planetary Science, Volume 22; Conference, Houston, TX, Mar. 18-22, 1991 (A92-30851 12-91), p. 87–100.

Smit, J., and Hertogen, J., 1980, An extraterrestrial event at the Cretaceous-Tertiary boundary: Nature, v. 285, no. 5762, p. 198–200, doi: 10.1038/285198a0.

Smit, J., Montanari, A., Swinburne, N.H.M., Alvarez, W., Hildebrand, A.R., Margolis, S. V, Claeys, P., Lowrie, W., and Asaro, F., 1992b, Tektite-bearing, deep-water clastic unit at the Cretaceous-Tertiary boundary in northeastern Mexico: Geology, v. 20, no. 2, p. 99–103.

Snedden, J.W., and Galloway, W.E., 2019, The Gulf of Mexico sedimentary basin: Depositional evolution and petroleum applications: Cambridge University Press.

Swisher, C.C., Grajales-Nishimura, J.M., Montanari, A., Margolis, S. V., Claeys, P., Alvarez, W., Renne, P., Cedillo-Pardo, E., Maurrasse, F.J.M.R., Curtis, G.H., Smit, J., and McWilliams, M.O., 1992, Coeval 40Ar/39Ar ages of 65.0 million years ago from Chicxulub crater melt rock and Cretaceous-Tertiary boundary tektites: Science, v. 257, no. 5072, p. 954–958, doi: 10.1126/science.257.5072.954.

Tschudy, R.H., Pillmore, C.L., Orth, C.J., Gilmore, J.S., and Knight, J.D., 1984, Disruption of the terrestrial plant ecosystem at the Cretaceous-Tertiary boundary, Western Interior: Science, v. 225, no. 4666, p. 1030–1032.

Tweto, O., 1979, Geologic map of Colorado: US Geological Survey.

Whitney, D.L., and Evans, B.W., 2010, Abbreviations for names of rock-forming minerals: American Mineralogist, v. 95, no. 1, p. 185–187, doi: 10.2138/am.2010.3371.

de Winter, N.J., and Claeys, P., 2017, Micro X-ray fluorescence (µXRF) line scanning on Cretaceous rudist bivalves: A new method for reproducible trace element profiles in bivalve calcite: Sedimentology, v. 64, no. 1, p. 231–251, doi: 10.1111/sed.12299.

De Winter, N.J., Sinnesael, M., Makarona, C., Vansteenberge, S., and Claeys, P., 2017, Trace element analyses of carbonates using portable and micro-X-ray fluorescence: Performance and optimization of measurement parameters and strategies: Journal of Analytical Atomic Spectrometry, v. 32, no. 6, p. 1211–1223, doi: 10.1039/c6ja00361c.

Wood, B.J., Smythe, D.J., and Harrison, T., 2019, The condensation temperatures of the elements: A reappraisal: American Mineralogist, v. 104, no. 6, p. 844–856, doi: 10.2138/am-2019-6852CCBY.

Wouters, S., Hulsbosch, N., Kaskes, P., Claeys, P., Dewaele, S., Melcher, F., Onuk, P., and Muchez, P., 2020, Late orogenic gold mineralization in the western domain of the Karagwe-Ankole Belt (Central Africa): Auriferous quartz veins from the Byumba deposit (Rwanda): Ore Geology Reviews, v. 125, doi: 10.1016/j.oregeorev.2020.103666.

Tables

#	Reference name	Details of institute	Material
1	BHVO-2	U.S. Geological Survey (USGS)	Basalt
2	RGM-2	U.S. Geological Survey (USGS)	Rhyolite
3	OREAS-20a	Ore Research and Exploration Pty.Ltd., Bayswater North, Australia (OREAS)	Granodiorite
4	GSP-2	U.S. Geological Survey (USGS)	Granodiorite
5	AGV-2	U.S. Geological Survey (USGS)	Andesite
6	AC-E	Centre de Recherches Petrographiques et Geochimiques (CRPG), Vandoeuvre-lès-Nancy, France	Granite
7	BCR-2	U.S. Geological Survey (USGS)	Basalt
8	OKUM	International Association of Geoanalysts, Nottingham, UK	Komatiite
9	GH	Centre de Recherches Petrographiques et Geochimiques (CRPG), Vandoeuvre-lès-Nancy, France	Granite
10	JA-1	Geological Survey of Japan, Higashi, Tsukuba, Ibaraki	Andesite
11	SARM-1	Council for Mineral Technology, Randburg, South Africa, (MINTEK)	Granite
12	RMG-1	U.S. Geological Survey (USGS)	Rhyolite
13	JR-2	Geological Survey of Japan, Higashi, Tsukuba, Ibaraki	Rhyolite

14	JR-1	Geological Survey of Japan, Higashi, Tsukuba, Ibaraki	Rhyolite
15	JB-2	Geological Survey of Japan, Higashi, Tsukuba, Ibaraki	Basalt

Table 1: List of certified reference materials used in this study.

#	Element or oxide	Slope value	Intercept	R^2
1	Na_2O (wt%)	0.7985	0.8022	0.9902
2	MgO (wt%)	1.0201	0.3914	0.9986
3	Al_2O_3 (wt%)	0.9994	0	0.9988
4	SiO_2 (wt%)	0.9325	6.7852	0.9929
5	K_2O (wt%)	0.9701	0.1741	0.9977
6	CaO (wt%)	1.1879	0	0.9980
7	TiO_2 (wt%)	1.0736	0	0.9993
8	MnO (wt%)	0.9750	0	0.9996
9	Fe_2O_3 (wt%)	0.8968	0	0.9997
10	Cl (ppm)	1.6902	0	0.9986
11	V (ppm)	0.9439	0	0.9923
12	Cr (ppm)	0.8334	0	0.9997
13	Ni (ppm)	0.9007	0	0.9908
14	Cu (ppm)	0.7171	0	0.9936
15	Zn (ppm)	0.7361	0	0.9961
16	Ga (ppm)	0.6268	0	0.9906
17	Rb (ppm)	0.9236	0	0.9982
18	Sr (ppm)	0.8182	0	0.9996
19	Y (ppm)	1.0142	12.12	0.9914
20	Zr (ppm)	0.8261	43.55	0.9953
21	Nb (ppm)	0.7595	0	0.9921
22	Ba (ppm)	1.0773	0	0.9924

Table 2: Slope, intercept and R^2 values for the µ-XRF regression lines for a selection of elements or oxides based on a calibration with the certified reference materials listed in Table 1 (see Fig. S2 for the calibration curves).

Supplementary Material

Disentangling impact ejecta dynamics using micro–X-ray fluorescence (µ-XRF): a case study from the terrestrial Cretaceous-Paleogene (K-Pg) boundary

Pim Kaskes[1,2], Roald Tagle[3], Mariia Rey[1], Steven Goderis[1], Sophie Decrée[4], Jan Smit[5], and Philippe Claeys[1]

[1] *Archaeology, Environmental Changes & Geo-Chemistry (AMGC), Vrije Universiteit Brussel, Pleinlaan 2, 1050 Brussels, Belgium.*
[2] *Laboratoire G-Time, Université Libre de Bruxelles, Av. F.D. Roosevelt 50, 1050 Brussels, Belgium.*
[3] *Bruker Nano Analytics GmbH, Am Studio 2d, 12489 Berlin, Germany.*
[4] *Institute of Natural Sciences – Geological Survey of Belgium, Vautierstraat 29, 1000, Brussels, Belgium.*
[5] *Department of Earth Sciences, Vrije Universiteit Amsterdam, De Boelelaan 1085, 1081 HV Amsterdam, Netherlands.*

Corresponding author: Pim Kaskes (pim.kaskes@vub.be)

Contents of this file

Table S1. Concentration data of major and trace elements of the Starkville-South (SVS) K-Pg boundary slab based on the two integrated-area linescan (IAL) profiles (at 25 µm stratigraphic resolution), following the µ-XRF calibration values displayed in Table 2. Data is available through the Zenodo online repository: https://zenodo.org/records/14552419.

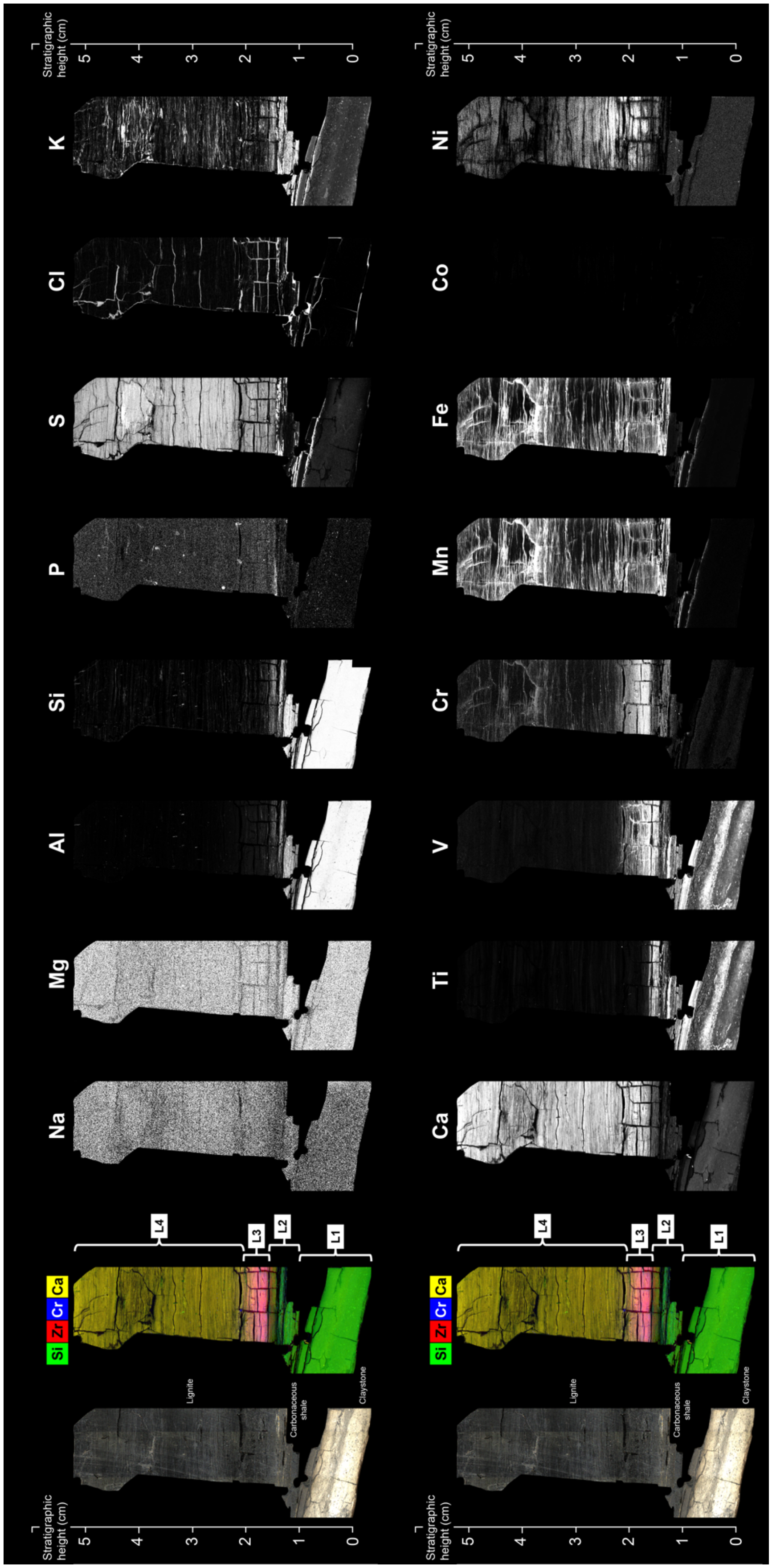
Stratigraphic height (cm)
Lignite
Carbonaceous shale
Claystone
Si Zr Cr Ca
L4
L3
L2
L1
Na
Mg
Al
Si
P
S
Cl
K
Ca
Ti
V
Cr
Mn
Fe
Co
Ni

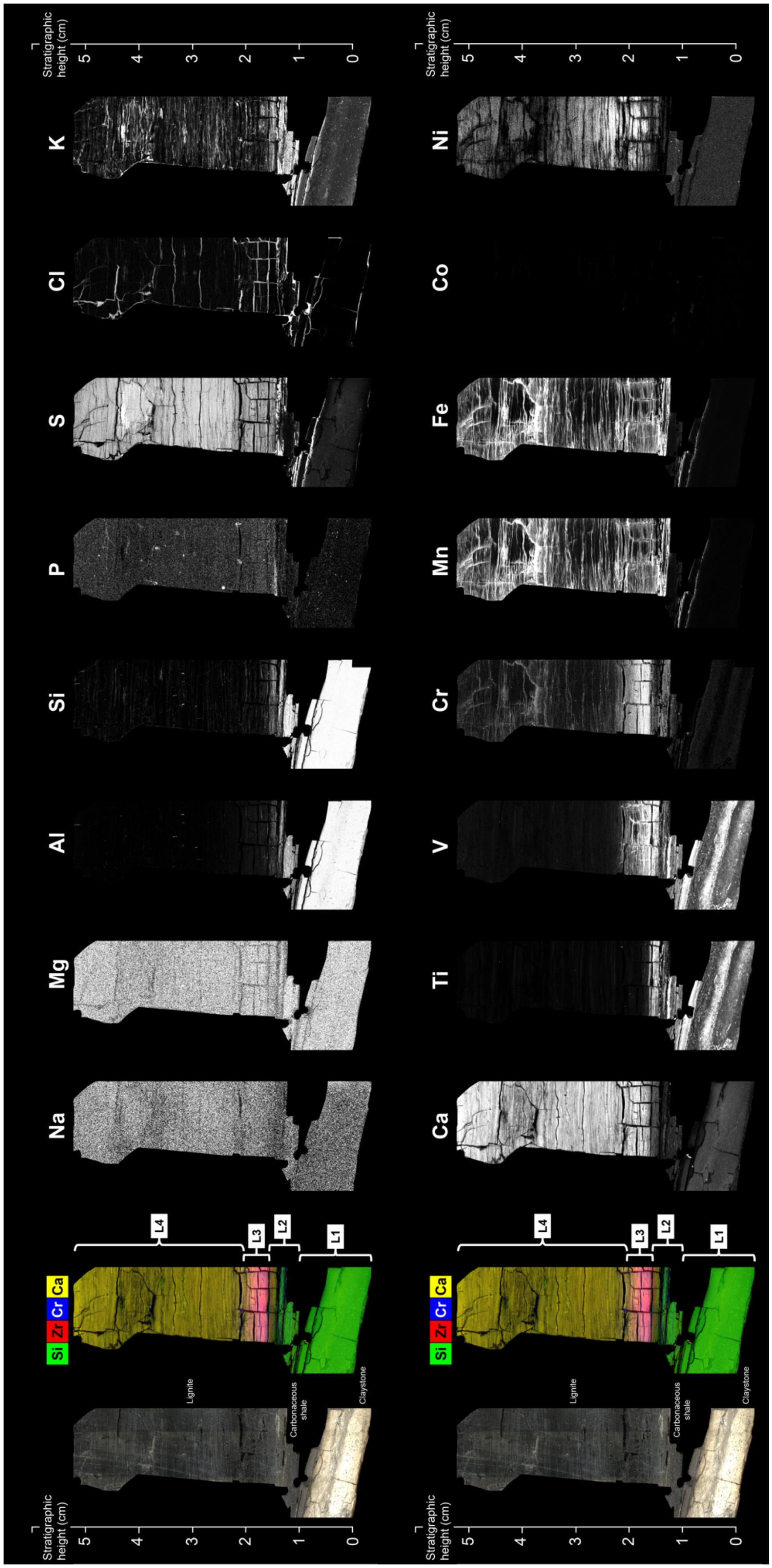
Stratigraphic height (cm)
Lignite
Carbonaceous shale
Claystone
Si
Zr
Cr
Ca
L1
L2
L3
L4
Na
Mg
Al
Si
P
S
Cl
K
Ca
Ti
V
Cr
Mn
Fe
Co
Ni

Figure S1. All µ-XRF single-element heatmaps of the SVS sample, showing the semi-quantitative distribution of 32 elements displayed as a black and white heatmap using deconvoluted settings in the Bruker TORNADO M4 software.

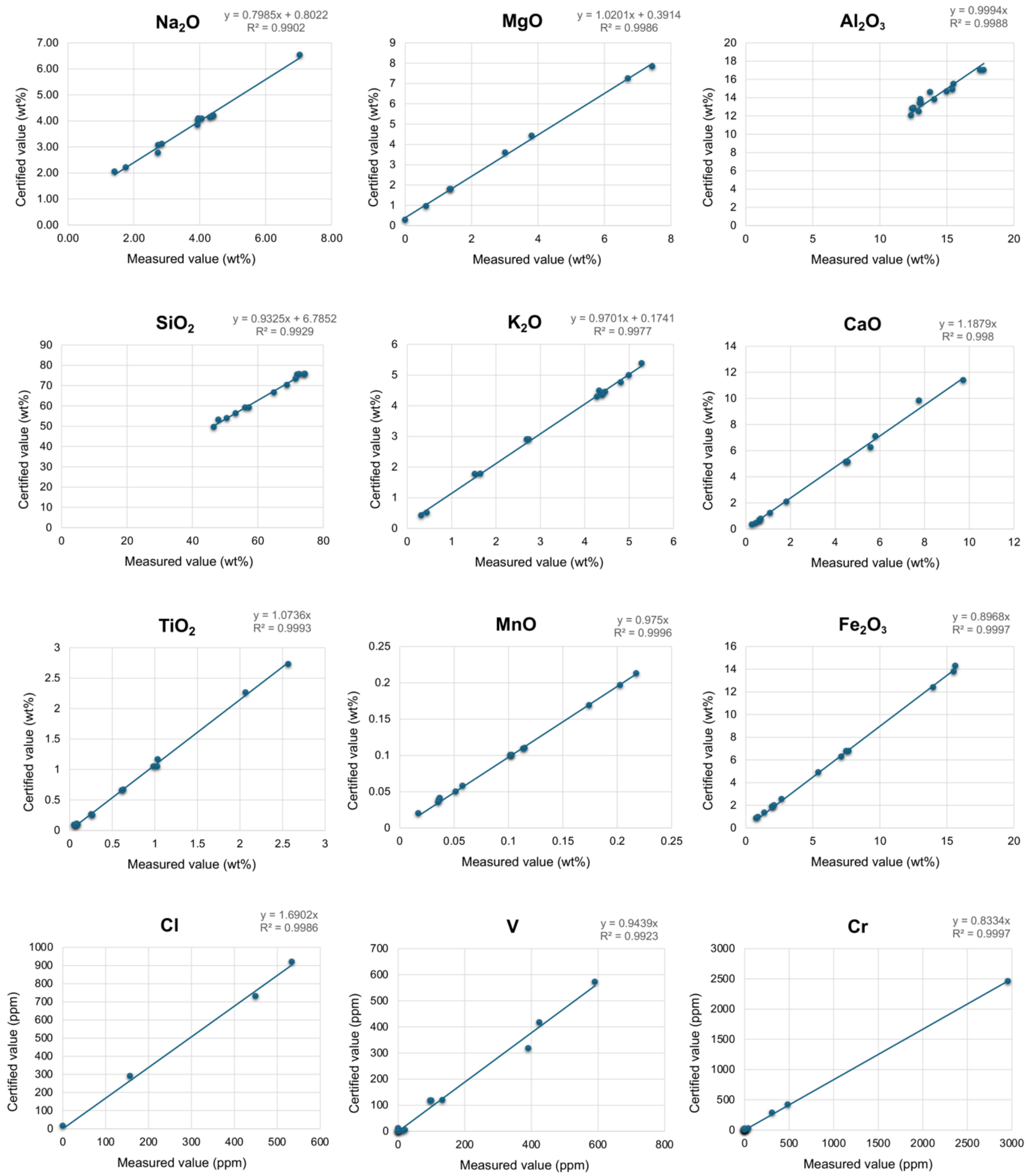

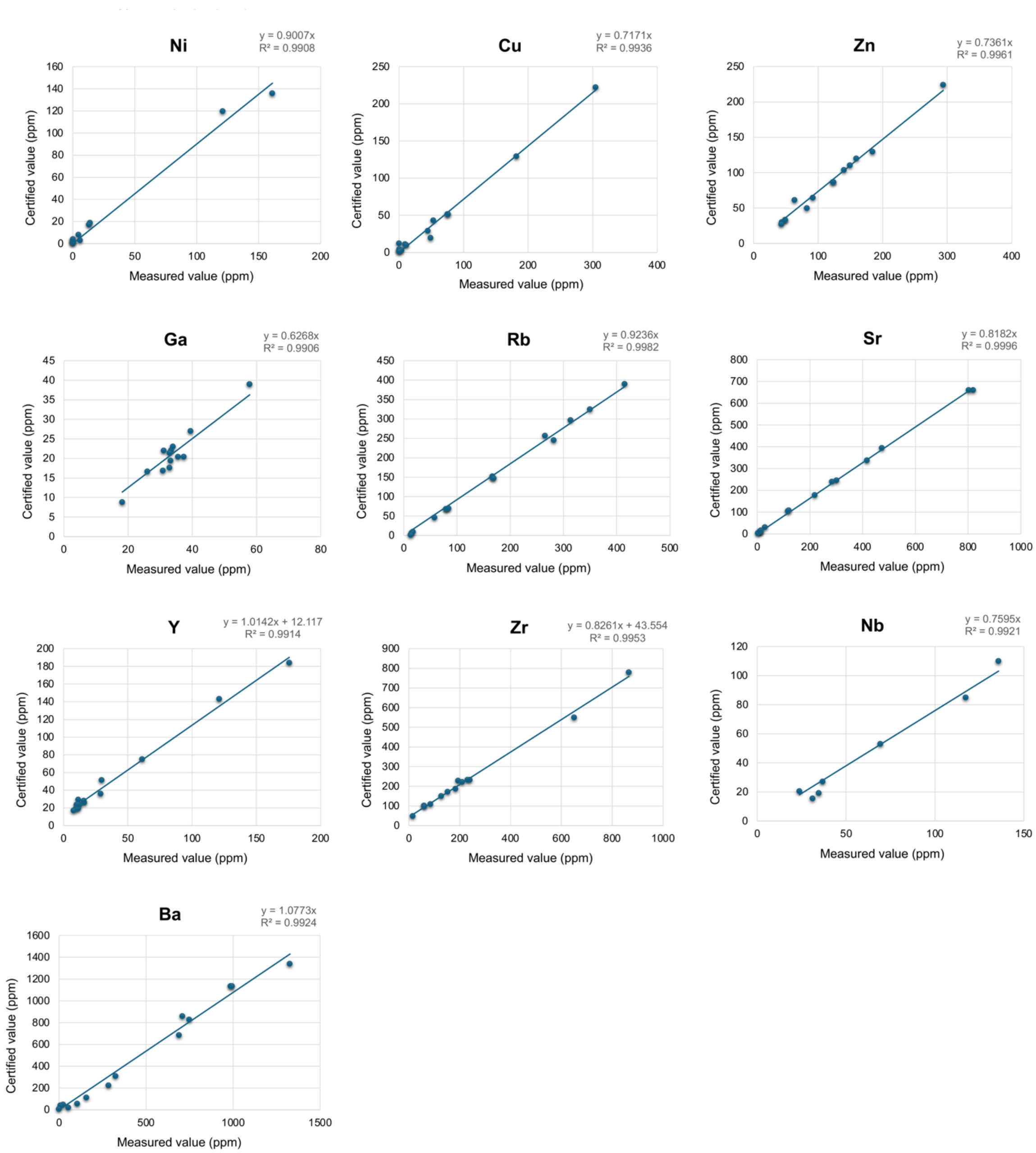

Figure S2. Calibration curves of all 22 elements studied in this µ-XRF project, based on extracted mass concentrations from the CRMs listed in Table 1.

See below:

Figure S3. Selected integrated-area linescan (IAL) profiles of major and trace elements. See Fig. 5 for the two IAL positions of the SVS sample.

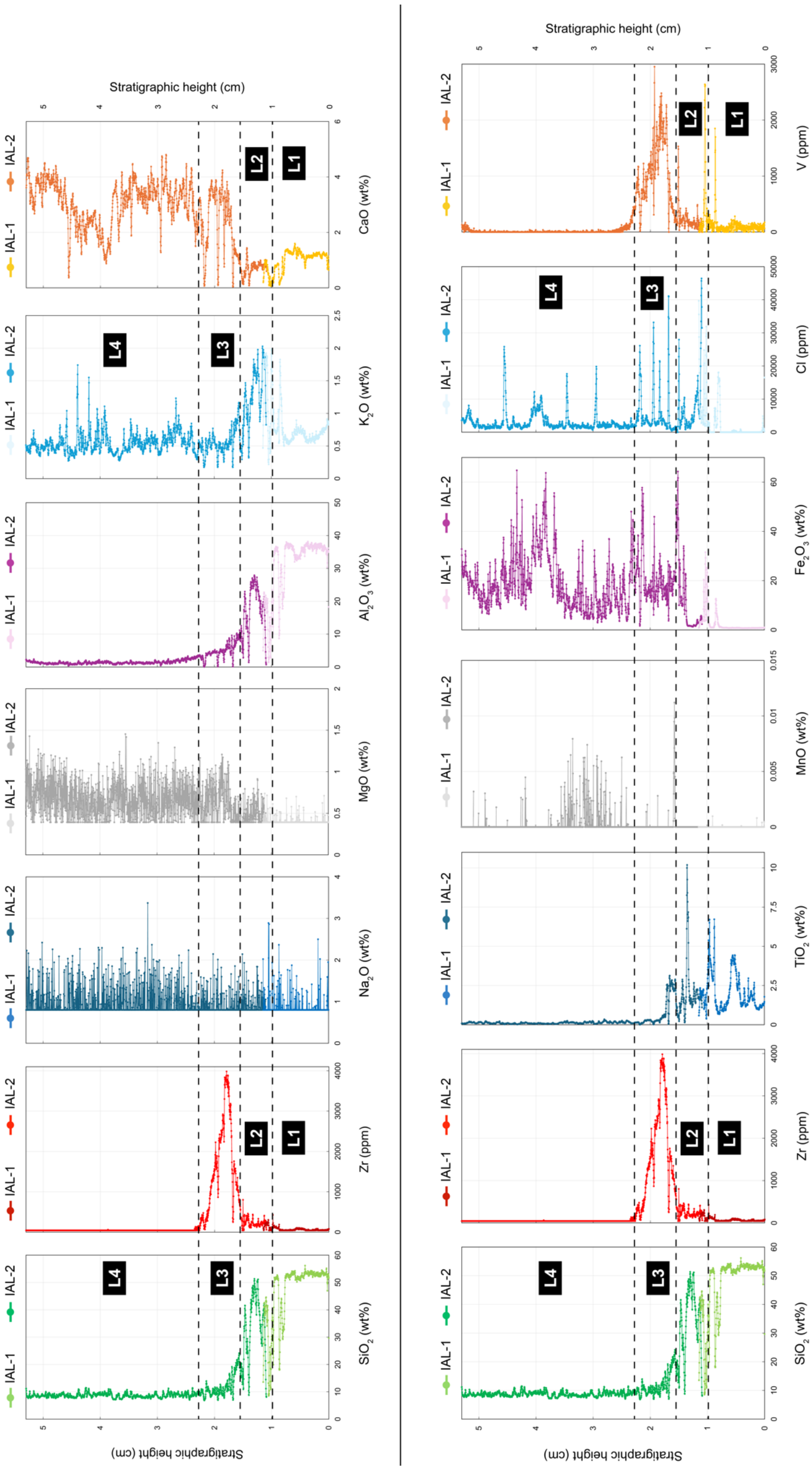
Stratigraphic height (cm)
IAL-1
IAL-2
L1
L2
L3
L4
CaO (wt%)
K2O (wt%)
Al2O3 (wt%)
MgO (wt%)
Na2O (wt%)
Zr (ppm)
SiO2 (wt%)
V (ppm)
Cl (ppm)
Fe2O3 (wt%)
MnO (wt%)
TiO2 (wt%)

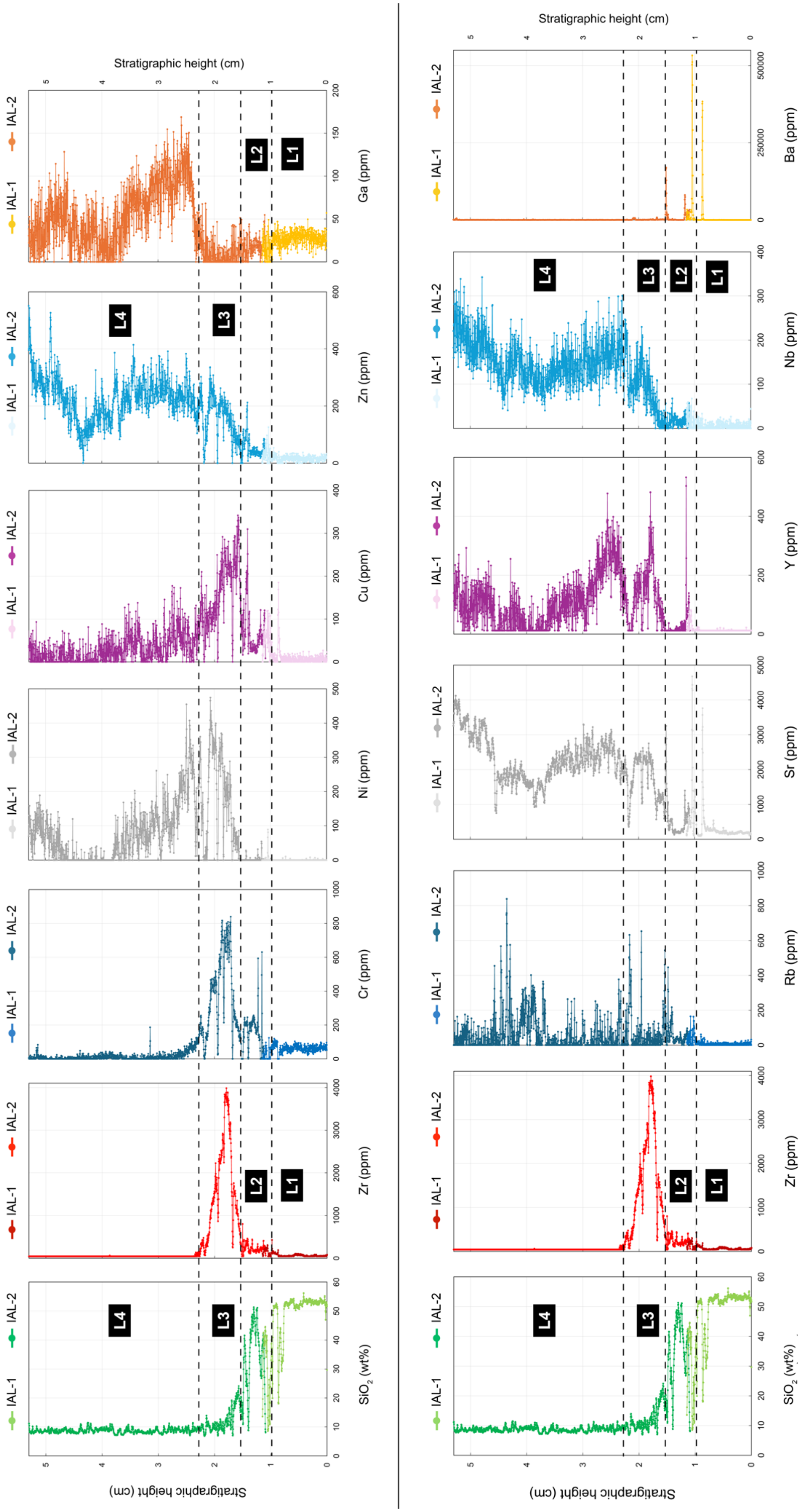
Stratigraphic height (cm)
Ga (ppm)
Zn (ppm)
Cu (ppm)
Ni (ppm)
Cr (ppm)
Zr (ppm)
SiO2 (wt%)
Ba (ppm)
Nb (ppm)
Y (ppm)
Sr (ppm)
Rb (ppm)
IAL-1
IAL-2
L1
L2
L3
L4